Central-difference schemes on non-uniform grids and their applications in large-eddy simulations of turbulent jets and jet flames

Haifeng Wang*, Stephen B. Pope, David A. Caughey

Sibley School of Mechanical and Aerospace Engineering, Cornell University, Ithaca, NY 14853, USA

Abstract

The conventional second-order central finite-difference schemes for discretizing the convection terms on non-uniform structured grids are revisited in the context of large-eddy simulations (LES) of turbulent flows. Two schemes are discussed: one is based on the standard finite-difference form on uniform grids (SCHEME-I) and the other is based on the Taylor series expansion (SCHEME-II). The two schemes are compared extensively in terms of the different numerical properties: accuracy, dissipation, dispersion, momentum-conservation, and energy-conservation. SCHEME-I is inherently conservative for momentum and is used in the design of different energy-conservative schemes, while, in general, SCHEME-II is not conservative for momentum and is not found so far to be able to produce any energy-conservative scheme. SCHEME-I is usually considered to be superior over SCHEME-II for LES due to the conservation property. However, it is found that the numerical solution by SCHEME-I may contain more energy than the exact solution and the numerical solution may oscillate strongly in spite of the energy-conservation of the scheme. On non-uniform grids, SCHEME-I introduces a second-order numerical diffusion term that can be anti-dissipative, resulting in local oscillations that can interact with the boundary conditions to cause the energy of the solution to increase. In contrast, SCHEME-II does not have such a numerical diffusion term, and it produces much less numerical oscillations than SCHEME-I for the test cases with grids expanding throughout in the flow direction. The performance of the two schemes is examined in the numerical simulations of a linear convection problem, a non-linear convection problem governed by the inviscid Burgers' equation, a laminar free jet, a constant-density turbulent jet, and a turbulent non-premixed jet flame. The superiority of SCHEME-II over SCHEME-I is clearly demonstrated in these test cases of different levels of complexity. SCHEME-II, which did not gain attention in past LES, is suggested for practical LES compared to the widely used SCHEME-I to capture the right level of turbulent kinetic energy.

Keywords: Large-eddy simulations, Numerical methods, central-difference schemes, non-uniform grids, turbulent jets and jet flames

Contents

1 Introduction **2**

2 Linear convection **5**

2.1 Discretization 5

*Corresponding author. Fax: +1 (607) 255 1222.
Email address: hw98@cornell.edu (Haifeng Wang)

2.2 Numerical accuracy 8
2.3 Numerical dissipation 9
2.4 Numerical dispersion 10
2.5 Momentum-conservation 11
2.6 Energy-conservation 13

3 Inviscid Burgers' equation 16
3.1 Discretization 16
3.2 Periodic test case 19
3.3 Non-periodic test case 20

4 Large eddy simulations (LES) 23
4.1 Numerical methods 23
4.2 Discretization of convection terms 24
4.3 Test case: constant-density laminar jet with *Re*=300 25

5 LES of a constant-density turbulent jet 27
5.1 Simulation details 27
5.2 Statistics 28
5.3 Effect on stability and cost 30

6 LES of turbulent jet flame (DLR Flame A) 32
6.1 Simulation details 32
6.2 Flow and turbulence fields 34
6.3 Combustion fields 34

7 Discussion 34

8 Conclusion 36

Appendix A Discrete conservations and modified PDEs 37

Appendix B Effect of grid transformation 39

Appendix C Effect of downstream boundary treatments 40

1. Introduction

Large eddy simulations (LES) have recently attracted great interest in the numerical simulations of turbulent flows, both for fundamental studies and for industrial applications. This is largely due to the rapidly increasing power of high-performance computers which makes the ever challenging LES computations affordable to more studies.

Significant advancement has been made in the development of numerical algorithms for LES. The principle of LES requires that the turbulent eddies down to the resolution scale (usually specified by the filter width Δ) need to be tracked with sufficient numerical accuracy, which poses a great challenge to the numerical schemes. In the past, high-order finite-difference schemes with good conservation property for LES have been developed. Morinishi et al. [1]

developed a family of fully conservative high-order finite-difference schemes for staggered uniform grids in Cartesian coordinates for incompressible flows. Vasilyev [2] generalized [1] to non-uniform grids, and Nicoud [3] generalized [1] to variable-density problems. Morinishi et al. [4] further developed high-order conservative schemes for staggered non-uniform grids in cylindrical coordinates for incompressible flows, and Desjardins et al. [5] extended the work to variable-density problems in cylindrical coordinates. Nagarajan et al. [6] proposed a high-order scheme for LES of compressible turbulent flows on Cartesian uniform grids based on the compact scheme of Lele [7]. Shishkina and Wagner [8] developed a fourth-order finite-volume scheme for incompressible flows on cylindrical staggered grids.

The use of the second-order finite-difference schemes in LES is controversial. Ghosal [9] showed that the numerical truncation errors from the low-order schemes may exceed the LES model terms. The dynamic analysis of Park and Mahesh [10], however, showed that the contribution of the LES model terms is much more significant than those of the finite-differencing and aliasing errors for LES with the energy-conserving second-order central-differencing schemes, which possibly justifies the use of the second-order schemes in LES. When predicting the low-order statistics (the first and second moments) that are of most interest in engineering applications, the second-order schemes are found satisfactory [11, 12], although they are not adequate for predicting higher-order statistics. The energy-conservative second-order schemes are also discussed in [1, 2, 4] when the higher-order schemes are concerned. The energy-conserving second-order schemes for incompressible flows on uniform grids were discussed in many articles, e.g., [13, 14, 15]. Ham et al. [16] developed a fully conservative second-order finite-difference scheme for incompressible flows on non-uniform grids. Fukagata and Kasagi [17] developed an energy-conservative second-order scheme for cylindrical coordinates. The second-order central finite-difference schemes are used widely in LES studies of turbulent flows [18, 19, 14, 20, 21, 22, 23] and turbulent combustion [24, 25, 26, 27, 28, 29, 30, 31, 32, 33, 34].

In spite of the wide use of second-order central-difference schemes, their important numerical properties on non-uniform grids are not fully comprehended in the context of LES. In this work, we revisit the second-order central-difference discretization. We limit our discussion to the schemes for the momentum-convection terms on staggered non-uniform structured grids. Two schemes that are used widely in the literature are discussed, and their numerical properties are analyzed, especially the numerical dissipation and the numerical energy production or dissipation that are missing from the literature.

The first scheme (SCHEME-I) is the direct extension of the central-difference scheme on uniform grids. On non-uniform grids, this finite-difference scheme is identical to the finite-volume scheme which is inherently conservative for momentum. It is probably this conservation property that makes this scheme very popular. It is used dominantly in the second-order accurate LES calculations on non-uniform grids (e.g., [18, 19, 14, 20, 21, 24, 25, 26, 27, 28, 29, 30, 31, 32, 33, 34]). The design of some energy-conserving schemes on non-uniform grids is based on SCHEME-I [1, 16]. However, it is shown later in this work that this scheme on non-uniform grids has a second-order numerical diffusion term which is dissipative or anti-dissipative depending on the local grid stretching and the flow direction. For expanding grid stretching in the flow direction, this scheme is anti-dissipative, resulting in oscillations that can interact with the boundary conditions to add energy to the numerical solution. Such a situation is often encountered in jet flow simulations in which the grid size is stretched in the axial flow direction to account for the increasing turbulence length scales. Such numerical diffusion of SCHEME-I adds numerical kinetic energy into the turbulence system for LES and makes the numerical simulation unreliable. To quantify the effect of such numerical diffusion, in this work we use jet flows (a laminar jet, a constant-density turbulent jet, and a turbulent jet flame) as test cases to reveal the poor performance of SCHEME-I in such flows and to demonstrate the capability of the second scheme. The second scheme (SCHEME-II) is based on the Taylor series expansion which gains almost no attention in recent LES studies on non-uniform grids. It is shown that SCHEME-II is free of the numerical diffusion and of the energy production or dissipation. In the various test cases of different levels of complexity in this work, SCHEME-II performs much better than the widely used SCHEME-I in LES of turbulent flows on non-uniform grids.

The above observations may look contradictory to the conclusions in the literature because SCHEME-I is well known for its inherent momentum-conservation and is used in the design of different energy-conserving schemes [1, 16], while SCHEME-II, in general, is neither momentum-conservative nor energy-conservative. The discrete conservations and the modified PDEs for SCHEME are reconciled in Appendix A.

SCHEME-I and SCHEME-II are identical on uniform grids. In some previous LES studies, the discretization strategy is to transform the equations from the physical space to the computational space and to discretize the equations in the computational space on uniform grids [2, 4, 5, 17]. Such a strategy does not reduce the strong oscillations in the numerical results by SCHEME-I on the expanding grids. Further analysis is presented in Appendix B.

The above two schemes on non-uniform grids have been known for more than forty years and have been discussed in many previous works. Crowder and Dalton [35] applied SCHEME-II in a model Poiseuille pipe flow to study the effectiveness of using non-uniform grids. In de Rivas [36], the truncation errors of SCHEME-I and SCHEME-II on non-uniform grids were studied, and it was shown that SCHEME-I had formally first-order truncation errors while it could achieve second-order accuracy on continuously stretched non-uniform grids, and SCHEME-II had formally second-order errors on any grid. Hoffman [37] also found that SCHEME-I had second-order accuracy for carefully chosen non-uniform grids by examining the truncation errors of SCHEME-I in the physical space and in the transformed computational space. Veldman and Rinzema [38] compared the performance of SCHEME-I and SCHEME-II in a one-dimensional boundary problem in which convection dominates. Based on their numerical experiments, they concluded that SCHEME-I reproduced the exact solution of the problem much better than SCHEME-II. Their conclusion is opposite to ours simply because their test case favors SCHEME-I in producing smooth numerical solutions due to the numerical diffusion introduced by the scheme (see Section 2.3 for details). Their work was followed by de Oliveira and Patricio [39] to study the numerical oscillations caused by the different schemes on non-uniform grids. The same test case was used, and hence they did not provide a complete understanding of the scheme's behavior on non-uniform grids. None of the above studies paid attention to the numerical dissipation properties of the two schemes or discussed the schemes in the context of LES which is vulnerable to numerical dissipation. In the existing literature, the understanding of the two schemes is incomplete and some conclusions are misleading.

This work is motivated by the situations mentioned above. We revisit the two widely known second-order central-difference schemes on non-uniform grids and provide comprehensive comparison of the schemes. In particular we compare the two schemes in LES studies of a turbulent jet and a jet flame.

This paper is organized as follows. In Section 2, the two schemes are discussed for a linear convection problem in terms of the different numerical properties: accuracy, dissipation, dispersion, momentum-conservation, and energy-conservation. In Section 3, the two schemes are compared in a non-linear convection problem governed by the inviscid Burgers' equation. In Section 4, we discuss the LES method used in this study. A laminar test case is presented to compare the performance of the two schemes. In Section 5, the LES of a constant-density turbulent jet is performed to compare the two schemes in this more complicated case. In Section 6, the LES of a turbulent jet flame (DLR Flame A) is performed to further compare the two schemes. Brief discussion is presented in Section 7. Finally, the conclusions are drawn in Section 8.

2. Linear convection

2.1. Discretization

We consider a one-dimensional linear convection test case

$$\frac{\partial u(x,t)}{\partial t} + \frac{\partial u(x,t)}{\partial x} = 0, \qquad (0 \leqslant x \leqslant 2\pi,\ 0 \leqslant t \leqslant T), \tag{1}$$

with a smooth initial condition $u(x, 0) = \sin(x)$, and with the periodic boundary condition (BC) (Problem-I)

$$u(x,t) = u(x + 2\pi, t), \tag{2}$$

or with the Dirichlet BC (Problem-II)

$$u(0,t) = sin(-t). \tag{3}$$

For hyperbolic problems (1), only one boundary condition is allowed for Problem-II (2). As discussed later, a numerical treatment at the downstream boundary $x = 2\pi$ is needed since central difference schemes are used in the following numerical solutions. The two problems with the different BCs have the same exact solution of $u(x, t) = \sin(x - t)$, i.e., a sine wave traveling to the right.

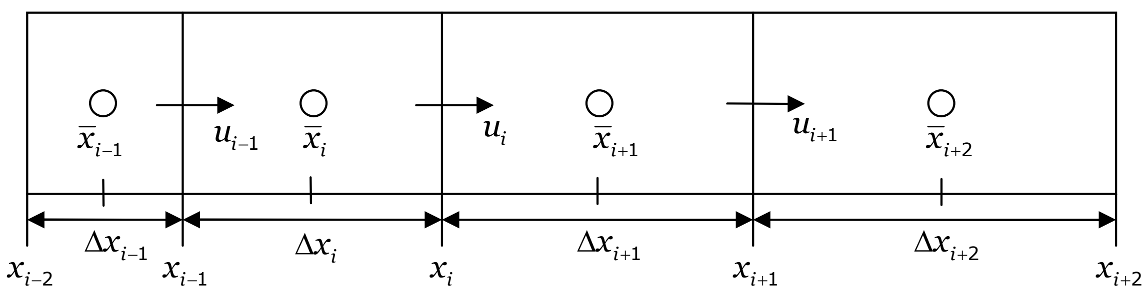

Figure 1: Non-uniform structured grid system.

We use a finite-difference method to solve equation (1) numerically. The grid system used in the numerical solution is shown in figure 1. The domain $[0, 2\pi]$ is divided into I non-uniform grid cells with the cell boundaries at x_i and the cell centers at $\overline{x}_i = (x_{i-1} + x_i)/2$ $(i = 1, \cdots, I)$. The grid spacing is $\Delta x_i = x_i - x_{i-1}$. The discrete variable $u_i = u(x_i, t)$ is located at the cell boundary, which is to mimic the grid staggering of the velocity components used widely in computational fluid dynamics (CFD).

A straightforward discretization of the spatial derivative (the convection term) in equation (1) is SCHEME-I:

$$\left(\frac{\partial u}{\partial x}\right)_i = \frac{u_{i+1/2} - u_{i-1/2}}{1/2(\Delta x_{i+1} + \Delta x_i)} = \frac{u_{i+1} - u_{i-1}}{\Delta x_{i+1} + \Delta x_i}, \tag{4}$$

where the spatial derivative is discretized at the cell boundary x_i, and the cell center value is interpolated linearly from the cell boundary values:

$$u_{i\pm1/2} = 1/2(u_{i\pm1} + u_i). \tag{5}$$

This discretization is the direct extension of the central-difference scheme on uniform grids. In this work, we focus on the discretization of the convection term, and keep the time derivative in the original form in the discretization. With

SCHEME-I in equation (4), the semi-discrete form of equation (1) is

$$\frac{du_i}{dt} + \frac{u_{i+1} - u_{i-1}}{\Delta x_{i+1} + \Delta x_i} = 0. \tag{6}$$

The second scheme (SCHEME-II) approximates the spatial derivative in equation (1) as

$$\left(\frac{\partial u}{\partial x}\right)_i = a_i u_{i+1/2} + b_i u_i + c_i u_{i-1/2}, \tag{7}$$

with coefficients a_i, b_i, and c_i to be determined.

By performing a Taylor series expansion, we have

$$u_{i\pm j} = u_i + \left(\frac{\partial u}{\partial x}\right)_i \left(x_{i\pm j} - x_i\right) + \frac{1}{2}\left(\frac{\partial^2 u}{\partial x^2}\right)_i \left(x_{i\pm j} - x_i\right)^2 + \frac{1}{6}\left(\frac{\partial^3 u}{\partial x^3}\right)_i \left(x_{i\pm j} - x_i\right)^3 + \cdots. \tag{8}$$

Substituting (8) with $j = 1/2$ into (7) and matching the terms up to the second-order derivative, we can derive SCHEME-II uniquely as follows

$$\begin{aligned}\left(\frac{\partial u}{\partial x}\right)_i &= \left(\frac{2}{\Delta x_{i+1}} - \frac{2}{\Delta x_{i+1} + \Delta x_i}\right) u_{i+1/2} + \left(\frac{2}{\Delta x_i} - \frac{2}{\Delta x_{i+1}}\right) u_i + \left(\frac{2}{\Delta x_{i+1} + \Delta x_i} - \frac{2}{\Delta x_i}\right) u_{i-1/2} \\ &= \left(\frac{1}{\Delta x_{i+1}} - \frac{1}{\Delta x_{i+1} + \Delta x_i}\right) u_{i+1} + \left(\frac{1}{\Delta x_i} - \frac{1}{\Delta x_{i+1}}\right) u_i + \left(\frac{1}{\Delta x_{i+1} + \Delta x_i} - \frac{1}{\Delta x_i}\right) u_{i-1},\end{aligned} \tag{9}$$

where the linear interpolation (5) is used. With SCHEME-II in the above, the semi-discretization of equation (1) is

$$\frac{du_i}{dt} + \left(\frac{1}{\Delta x_{i+1}} - \frac{1}{\Delta x_{i+1} + \Delta x_i}\right) u_{i+1} + \left(\frac{1}{\Delta x_i} - \frac{1}{\Delta x_{i+1}}\right) u_i + \left(\frac{1}{\Delta x_{i+1} + \Delta x_i} - \frac{1}{\Delta x_i}\right) u_{i-1} = 0. \tag{10}$$

It can be seen that the difference between SCHEME-I and SCHEME-II vanishes when uniform grids ($\Delta x_i = \Delta x_{i+1}$) are used.

The modified PDEs corresponding to the semi-discrete equations (6) and (10) provide valuable insight into the schemes' properties. Substituting the Taylor series expansion in (8) with $j = 1$ to the discrete equations (6) and (10), we can derive their modified PDEs.

The modified PDE for equation (6) (SCHEME-I) is

$$\frac{\partial u}{\partial t} + \frac{\partial u}{\partial x} = -\frac{1}{2}\left(\Delta x_{i+1} - \Delta x_i\right)\frac{\partial^2 u}{\partial x^2} - \frac{1}{6}\frac{\Delta x_{i+1}^3 + \Delta x_i^3}{\Delta x_{i+1} + \Delta x_i}\frac{\partial^3 u}{\partial x^3} + O\left(\Delta x^3\right), \tag{11}$$

and the modified PDE for equation (10) (SCHEME-II) is

$$\frac{\partial u}{\partial t} + \frac{\partial u}{\partial x} = -\frac{1}{6}\Delta x_{i+1}\Delta x_i \frac{\partial^3 u}{\partial x^3} + O\left(\Delta x^3\right), \tag{12}$$

where for simplicity the subscript i is omitted from all the derivatives, and Δx (without a subscript) is a nominal grid size to indicate the order of magnitude.

In the following, we compare the different numerical properties of SCHEME-I and SCHEME-II. In the numerical tests, the second-order Crank-Nicholson scheme is used to approximate the temporal derivative in the semi-discrete equations (6) and (10). For problem-II (3), we specially treat the downstream boundary as a Dirichlet BC and impose

$$u(2\pi, t) = sin(-t) \tag{13}$$

from the exact solution. The effect of the different downstream boundary treatments is evaluated in Appendix C, and no qualitative effect on the numerical solutions is found.

Three different grids are used in the numerical tests: the exponential grid (EG), the polynomial grid (PG), and the matching grid (MG) that matches on the ends.

Exponential Grid (EG): The exponential grid is defined by

$$x_i = 2\pi \left[\exp\left(\frac{\alpha i}{I}\right) - 1\right] \Big/ \left[\exp(\alpha) - 1\right] \qquad (i = 0, \cdots, I), \tag{14}$$

where α is a parameter to specify the grid stretching rate and I is the number of the grid cells. We define the grid size ratio $\gamma_i = \Delta x_{i+1}/\Delta x_i$. Substituting equation (14) to γ_i, we have

$$\gamma_i = \frac{\Delta x_{i+1}}{\Delta x_i} = \frac{x_{i+1} - x_i}{x_i - x_{i-1}} = \exp\left(\frac{\alpha}{I}\right), \tag{15}$$

which is constant for the exponential grids. The ratio of the largest and smallest grid size is

$$\beta = \frac{\Delta x_I}{\Delta x_1} = \frac{x_I - x_{I-1}}{x_1 - x_0} = \exp\left[\alpha\left(1 - \frac{1}{I}\right)\right]. \tag{16}$$

When the number of grid cells I tends to infinity, the ratio β of the largest and smallest grid cells for the exponential grid tends to $\exp(\alpha)$.

Polynomial Grid (PG): The polynomial grid is defined by

$$x_i = 2\pi \left(\frac{i}{I}\right)^p \qquad (i = 0, \cdots, I), \tag{17}$$

where p is a parameter to specify the grid stretching. We consider a special case $p = 2$, and the ratio γ_i is

$$\gamma_i = \frac{x_{i+1} - x_i}{x_i - x_{i-1}} = \frac{2\pi\left(\frac{i+1}{I}\right)^2 - 2\pi\left(\frac{i}{I}\right)^2}{2\pi\left(\frac{i}{I}\right)^2 - 2\pi\left(\frac{i-1}{I}\right)^2} = 1 + \frac{1}{i - 1/2}, \tag{18}$$

which is not a constant. The maximum stretching occurs at $i = 1$ at which $\gamma_1 = 3$, and the minimum stretching occurs at $i = I - 1$ at which $\gamma_{I-1} = 1 + 1/(I - 3/2)$. When the number of grids cells I tends to infinity, the maximum stretching of the grid does not change ($\gamma_1 = 3$), and the minimum stretching reduces to $\gamma_\infty = 1$. The ratio of the largest and smallest grid size is $\beta = 2I - 1$ which becomes infinite when I tends to infinity. For the polynomial grid (17) with $p = 2$, the difference of the grid size is constant, i.e., $\Delta x_{i+1} - \Delta x_i = 4\pi/I^2$.

Matching Grid (MG): The matching grid is defined by the exponential grids for ($i \leqslant I/2$) and reflecting the grid sizes to $i > I/2$ so that $\Delta x_{I-i} = \Delta x_{i+1}$ ($i = 0, \cdots, I/2$). The grid spacing then varies smoothly from one end to the other and the periodic BC can be properly imposed.

In this work, the EG and PG grids are only used when Problem-II (with the Dirichlet BC in (3)) is solved. it is not straightforward to solve Problem-I (with periodic BCs in (2)) on EG and PG grids without extra boundary treatment.

The MG grids can be used for solving both Problem-I and Problem-II straightforwardly.

2.2. Numerical accuracy

From the modified PDE (11), we can see that in general SCHEME-I is formally first-order accurate due to the leading truncation error term on the order of $O(|\Delta x_{i+1} - \Delta x_i|)$. However, as shown in many previous works (e.g., in [36, 37] and in the textbook [40]), SCHEME-I has second-order accuracy on a stretched grid satisfying $|\Delta x_{i+1} - \Delta x_i| = O(\Delta x^2)$. SCHEME-II is formally second-order accurate for any grid according to the modified PDE (12). For further discussion on the numerical accuracy of the schemes on non-uniform grids, the reader is referred to [36, 37, 40].

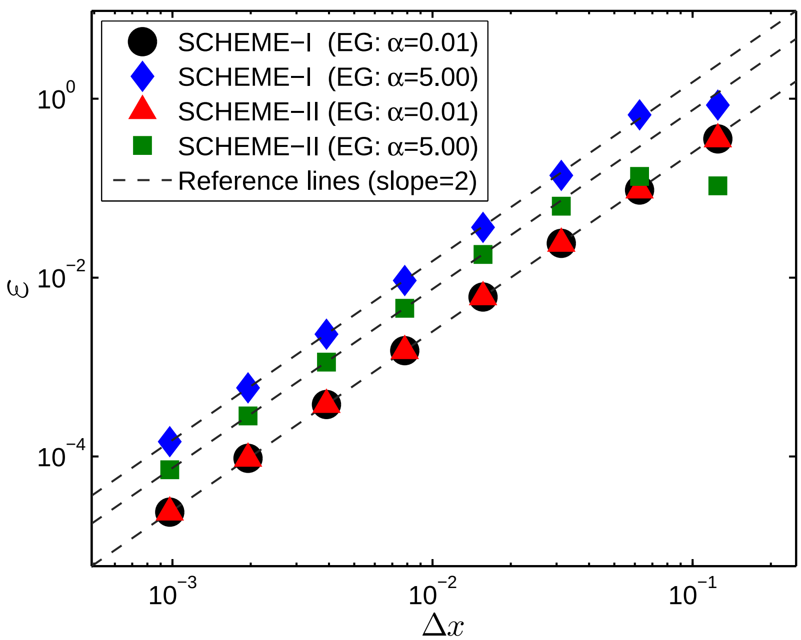

Figure 2: Numerical error ε against the nominal grid size Δx with SCHEME-I and SCHEME-II on the exponential grids with the different grid stretching rates for Problem-II (with the Dirichlet BC).

Here we present numerical tests to examine the effect of the grid stretching on the numerical accuracy. Problem-II (3) on the EG grids is solved numerically with SCHEME-I and SCHEME-II, and the numerical results are compared in figure 2. Two different grid stretching rates are used: a low stretching rate ($\alpha = 0.01$, $\exp(\alpha) = 1.01$) and a high stretching rate ($\alpha = 5.0$, $\exp(\alpha) = 148.41$). The numerical solutions are marched to the stopping time $T = 2\pi$ (one period) with the initial condition $u(x, 0) = sin(x)$, and the numerical errors are measured at the stopping time as

$$\varepsilon = \sqrt{\frac{1}{I}\sum_{i=1}^{I}\left(u_i(T) - u(x_i, T)\right)^2} \tag{19}$$

with $u_i(T)$ and $u(x_i, T)$ being the numerical solution and exact solution at time T, respectively. The nominal grid size Δx is specified as $\Delta x = 2\pi/I$ in figure 2.

From figure 2, for the low grid stretching rate ($\alpha = 0.01$) with which the grid is almost uniform, we can see that the results of SCHEME-I and SCHEME-II are indistinguishable because SCHEME-I and SCHEME-II are identical on uniform grids. For the high grid stretching rate ($\alpha = 5.0$), the numerical error ε of SCHEME-II is about half of that of SCHEME-I. For all the test results, the numerical error ε shows second-order decay ($\varepsilon \sim O(\Delta x^2)$) as the grids are refined compared to the reference lines with slope two in figure 2, indicating the second-order accuracy of both schemes on the grids considered.

2.3. Numerical dissipation

From the modified PDE (11) for SCHEME-I, we can see that this scheme introduces a second-order numerical diffusion (dissipation) term (the first term on the right-hand side of equation (11) with a numerical diffusivity $\nu_{\text{num}} = -1/2(\Delta x_{i+1} - \Delta x_i)$) which is dissipative or anti-dissipative depending on the local grid stretching. For grids expanding in the flow direction ($\Delta x_{i+1} > \Delta x_i$), the numerical diffusivity ν_{mum} is negative and hence this term is anit-dissipative. Any numerical oscillations appearing in the numerical solutions are amplified by the negative numerical diffusion, and hence the numerical solutions are potentially unstable. For grids shrinking in the flow direction ($\Delta x_{i+1} < \Delta x_i$), the numerical diffusivity ν_{num} is positive and the term is dissipative. This dissipative nature of the numerical schemes is often useful in CFD to help stabilize the numerical solutions, while excessive numerical diffusion may damp the numerical solutions too much and hence jeopardize the numerical accuracy. In contrast, SCHEME-II does not have the second-order numerical diffusion term according to the modified PDE (12).

The above numerical dissipation property of SCHEME-I was not fully appreciated in any previous work although the modified PDE for SCHEME-I was often mentioned when discussing the numerical accuracy (e.g., [36, 37, 38, 39, 40]). In the work by Veldman and Rinzema [38] and by de Oliveira and Patricio [39], SCHEME-I and SCHEME-II were compared in a convection-diffusion boundary layer problem with a grid shrinking in the flow direction. In this case, the numerical diffusivity ν_{num} introduced by SCHEME-I is positive, and hence SCHEME-I is inherently dissipative to suppress the numerical oscillations. Veldman and Rinzema [38] concluded that SCHEME-I is better than SCHEME-II, which is only partially correct. De Oliveira and Patricio [39] also obtained smoother numerical solutions using SCHEME-I than those using SCHEME-II, and further observed the excessive numerical diffusion when the numerical diffusivity ν_{num} is comparable to the diffusivity in the model equation. None of the previous works compared the two schemes on grids expanding in the flow direction.

Here we perform a test to compare the schemes on grids expanding in the flow direction to examine the numerical oscillations produced by the schemes. Problem-II (3) is solved numerically on the EG grid in equation (14) with a high grid stretching rate $\alpha = 3.6$ ($\exp(\alpha) \approx 36.6$) and with the number of grid cells $I = 50$. The numerical simulations are marched to the stopping time $T = 10\pi$, i.e., returning to the initial condition after five periods. The numerical solutions at $T = 10\pi$ are compared in figure 3 with SCHEME-I and SCHEME-II on the EG grid expanding in the flow direction. Excessive numerical oscillations are observed in the numerical solution (circles in figure 3) by SCHEME-I due to the amplification of the numerical oscillations by SCHEME-I on the given grids. In contrast, the numerical solution by SCHEME-II (diamonds in figure 3) reproduces the exact smooth solution (solid line in figure 3) very well. The numerical oscillations with the wave length of two grid cells in figure 3 are caused by the numerical dispersion discussed in Section 2.4 below. For grids expanding in the flow direction, SCHEME-I consistently amplifies the magnitude of these numerical oscillations, while SCHEME-II does not alter the magnitude of the oscillations. (SCHEME-II has high-order dissipation terms (fourth-order derivatives and higher) in the truncation errors in equation (12) which produces a dissipative or anti-dissipative effect. This is in contrast to the dissipative-free nature of the central-difference schemes on uniform grids. The dissipation effect of SCHEME-II is of high-order and is not discussed in this work for the second-order schemes.)

The above numerical dissipation property of SCHEME-I makes it not appropriate for LES. However, SCHEME-I is widely used in LES (e.g., [18, 19, 14, 20, 21, 24, 25, 26, 27, 28, 29, 30, 31, 32, 33, 34]). The negative numerical

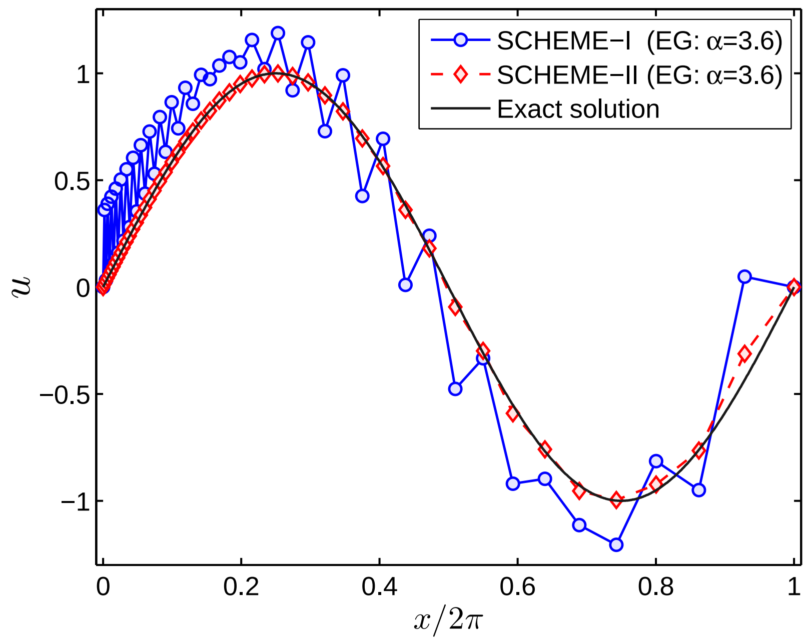

Figure 3: Numerical solution u at the stopping time $T = 10\pi$ against the position $x/(2\pi)$ with SCHEME-I and SCHEME-II on the EG grid in equation (14) for Problem-II (with the Dirichlet BC).

diffusion for grids expanding in the flow direction amplifies the numerical oscillations and makes the LES solutions tend to unstable. The magnitude of the numerical diffusion (no matter positive or negative) is on the order of Δx^2 which is comparable to the LES model terms and hence makes the LES results unreliable. SCHEME-II is more appropriate for LES compared to SCHEME-I since it does not have the second-order numerical diffusion terms in the truncation errors.

Another way to address the non-uniformity is to convert the problem in physical space to a problem in the computational space so that the uniform grids can be used. As discussed in Appendix B, such practice is similar to considering the problem in physical space by using SCHEME-I and hence is not recommended for LES.

2.4. Numerical dispersion

An intrinsic difficulty of using central-difference schemes for the first-order derivative is the numerical dispersion which causes the numerical oscillations, e.g., the oscillations with the wave length of two grid sizes in figure 3 for both SCHEME-I and SCHEME-II. The numerical oscillations produced by SCHEME-I are significantly amplified by the numerical dissipation discussed in the above Section 2.3. The numerical oscillations produced by SCHEME-II are small for the test case in figure 3 and are only evident in the region with the course grids (near $x = 2\pi$). It is not straightforward to compare the numerical oscillations caused by SCHEME-I and SCHEME-II in figure 3 due to the interference by the numerical dissipation. Instead we directly compare the magnitude of the dispersion term in the modified PDEs (11) and (12). For SCHEME-I, the magnitude of the numerical dispersion term (the second term on the right-hand side of equation (11)) is

$$H_1 = \left| -\frac{1}{6}\frac{\Delta x_{i+1}^3 + \Delta x_i^3}{\Delta x_{i+1} + \Delta x_i}\frac{\partial^3 u}{\partial x^3} \right| = \frac{1}{6}\left|\frac{\partial^3 u}{\partial x^3}\right|\left[\Delta x_{i+1}\Delta x_i + (\Delta x_{i+1} - \Delta x_i)^2\right], \tag{20}$$

and for SCHEME-II the magnitude of the numerical dispersion term is

$$H_2 = \left| -\frac{1}{6}\Delta x_{i+1}\Delta x_i \frac{\partial^3 u}{\partial x^3} \right| \le \frac{1}{6}\left|\frac{\partial^3 u}{\partial x^3}\right| \left[\Delta x_{i+1}\Delta x_i + (\Delta x_{i+1} - \Delta x_i)^2\right] = H_1. \tag{21}$$

Therefore the numerical dispersion error H_2 in SCHEME-II is smaller in magnitude than H_1 in SCHEME-I. The more stretched the grids are, the greater the difference is of the dispersion errors H_1 and H_2.

2.5. Momentum-conservation

The conservation principle of equation (1) imposes an additional constraint on the finite-difference schemes, i.e., the schemes are able to mimic the conservation principle on the discrete level [1]. Several conservative discrete operators were introduced to discretize the Navier-Stokes equations [1, 16]. SCHEME-I (4) is the conservative discrete operator on non-uniform grids [16].

Integrating the conservation equation (1) on $[0, 2\pi]$, we obtain

$$\frac{d}{dt}\int_0^{2\pi} u(x,t)dx = u(0,t) - u(2\pi,t). \tag{22}$$

So the net change of the integral $\int_0^{2\pi} u(x,t)dx$ (total momentum) is caused only by the difference of the momentum-fluxes on the boundaries, $u(0,t) - u(2\pi,t)$. For Problem-I (2), we have $u(0,t) = u(2\pi,t)$, hence

$$\frac{d}{dt}\int_0^{2\pi} u(x,t)dx = 0. \tag{23}$$

For Problem-II (3) with the downstream boundary treatment (13), we also have the result in equation (23). Thus the momentum-conservation requires $\int_0^{2\pi} u(x,t)dx =$ const at all times over the domain. We simply approximate the integral $\int_0^{2\pi} u(x,t)dx$ by

$$C = \sum_{i=1}^{I} \frac{1}{2}(u_{i-1} + u_i)\Delta x_i. \tag{24}$$

on the grid system in figure 1. Performing the summation (24) for SCHEME-I in equation (6), we obtain

$$\begin{aligned}
\frac{dC}{dt} &= \frac{d}{dt}\left[\frac{1}{2}u_0\Delta x_1 + \sum_{i=1}^{I-1}\frac{1}{2}(\Delta x_i + \Delta x_{i+1})u_i + \frac{1}{2}u_I\Delta x_I\right] \\
&= \left[\frac{1}{2}\Delta x_1\frac{du_0}{dt} + \frac{1}{2}(u_0 + u_1)\right] - \left[\frac{1}{2}(u_{I-1} + u_I) - \frac{1}{2}\Delta x_I\frac{du_I}{dt}\right].
\end{aligned} \tag{25}$$

The above equation shows that the net change of C by SCHEME-I is caused only by the difference of the boundary values, i.e, SCHEME-I mimics the conservation law in equation (22) on the discrete level. Hence, SCHEME-I is conservative for the momentum. For Problem-I, we can obtain that $dC/dt = 0$ and $C =$ const by imposing the periodic BC $u_{I+i} = u_i$ and $\Delta x_{I+i} = \Delta x_i$; for Problem-II, we obtain that $dC/dt = (u_0 + u_1)/2 - (u_{I-1} + u_I)/2 \neq 0$ due to the non-periodicity of the numerical solutions.

For SCHEME-II in equation (10), we can write down the summation as

$$\frac{dC}{dt} = \frac{1}{2}\Delta x_1\frac{du_0}{dt} + \sum_{i=1}^{I-1}\frac{1}{2}\left[(u_{i+1} - u_i)/\gamma_i + (u_i - u_{i-1})\gamma_i\right] + \frac{1}{2}\Delta x_I\frac{du_I}{dt}, \tag{26}$$

where $\gamma_i = \Delta x_{i+1}/\Delta x_i$. In general the righthand side of equation (26) depends on the numerical solutions on all grid points except some special cases, e.g. γ_i=const which is the EG grid in equation (14). Thus, for arbitrary grids, SCHEME-II does not conserve the momentum on the discrete level exactly.

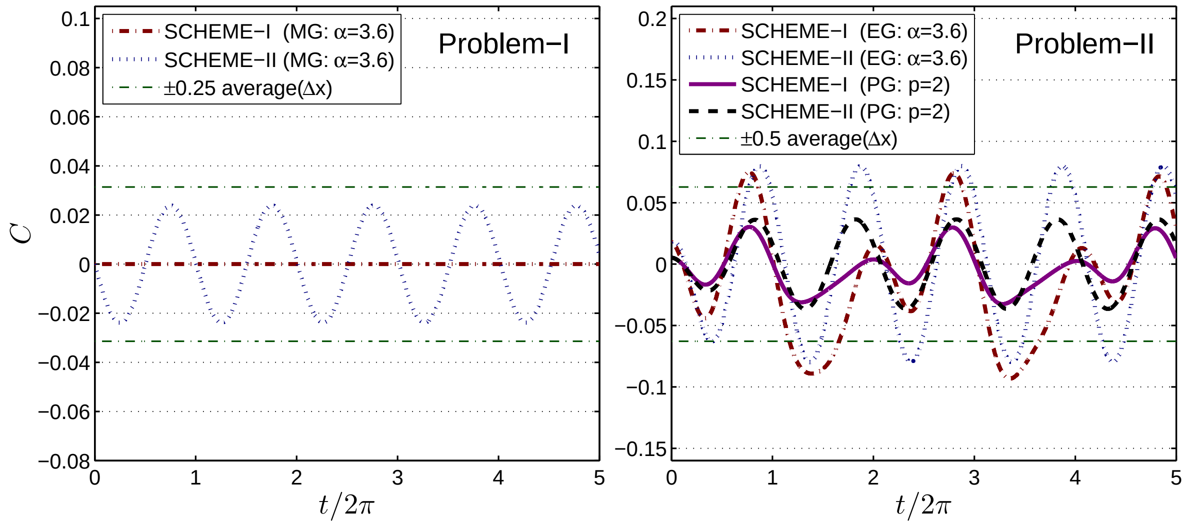

Figure 4: The measurement of the momentum-conservation C against time $t/(2\pi)$ with SCHEME-I and SCHEME-II on the MG grid for Problem-I (left plot) and on the EG grid and the PG grid for Problem-II (right plot). The thin dash-dotted lines are reference lines showing the difference from C=0.

In the following, we perform the numerical tests to examine the momentum-conservation of the two schemes. The number of the grid cells is $I = 50$ and the numerical solutions are marched to $T = 10\pi$ from the initial condition. The time series of C with the different schemes for Problem-I and Problem-II are compared in figure 4.

For Problem-I (left plot of figure 4), the MG grid is used with $\alpha = 3.6$ in equation (14). The momentum-conservation requires C=0 at all times for Problem-I. The values of C by SCHEME-I (dash-dotted line) are zero throughout the time, confirming the momentum-conservation of the scheme. The values of C by SCHEME-II (dotted line) are not zero exactly, indicating the violation of the momentum-conservation by the scheme. The violation, however, does not grow with time, and varies around zero periodically in time.

For Problem-II (right plot of figure 4), two different grids are compared for SCHEME-I and SCHEME-II for the momentum-conservation: the EG grid in equation (14) ($\alpha = 3.6$, γ_i = const) and the PG grid in equation (17) ($p = 2$, $1 < \gamma_i \leqslant 3$). For this problem, the values of C are not zero for both schemes according to equations (25) and (26). From the right plot of figure 4, we can make the following observations:

1. The values of C from all four test cases vary periodically in time. The magnitude of C by SCHEME-I is about twice of that by SCHEME-II for both the EG and PG grids;
2. Although the predicted values for C by SCHEME-I and SCHEME-II look similar, they are qualitatively different. The non-zero values of C by SCHEME-I (solid and dash-dotted lines) are caused only by the non-zero net change of the momentum-fluxes on the boundaries as shown in equation (25). This does not contradict the fact that SCHEME-I conserves momentum in spite of the non-zero values of C predicted by the scheme. The non-zero values of C on the EG grid by SCHEME-II (dotted line) are also caused only by the non-zero net change of the momentum-fluxes on the boundaries as shown in equation (26) due to the fact that SCHEME-II conserves momentum on the EG grid. The non-zero values of C on the PG grid by SCHEME-II (dashed line),

however, are caused by the violation of the momentum-conservation by the scheme as well as by the net change of the momentum-fluxes on the boundaries;

3. For Problem-II, the violation of the momentum-conservation seems comparable in magnitude to the boundary effect, and the non-momentum-conservative SCHEME-II does not show disadvantages over the momentum-conservative SCHEME-I in predicting the values of total momentum C.

The intrinsic momentum-conservation property of SCHEME-I is perhaps the main reason for its wide use in CFD. Here based on the analysis and the numerical tests, we see that, for Problem-II, SCHEME-II (non-momentum-conservative) has comparable performance to SCHEME-I in predicting the values of C for the linear convection problem.

2.6. Energy-conservation

From figure 3, we can see that the numerical solution by SCHEME-I oscillates strongly, while that by SCHEME-II is smoother and closer to the exact solution. An immediate question to follow is whether SCHEME-I conserves energy in addition to the momentum-conservation. The energy-conservation is often recommended for designing numerical schemes for LES.

The conservation law in equation (1) implies conservation of the energy $u^2(x,t)/2$, i.e.,

$$\frac{\partial u^2(x,t)}{\partial t} + \frac{\partial u^2(x,t)}{\partial x} = 0 \qquad (0 \leqslant x \leqslant 2\pi,\ 0 \leqslant t \leqslant T). \tag{27}$$

So similar to equations (25), the energy conservation implies

$$\frac{d}{dt}\int_0^{2\pi} u^2(x,t)dx = u^2(0,t) - u^2(2\pi,t), \tag{28}$$

i.e., the net change of the total energy is due to the difference of the energy-fluxes on the boundaries. For both Problem-I and Problem-II, we have $u(0,t) = u(2\pi,t) = sin(-t)$, so the energy-conservation yields

$$\frac{d}{dt}\int_0^{2\pi} u^2(x,t)dx = 0 \quad \text{and} \quad \int_0^{2\pi} u^2(x,t)dx = \text{const.} \tag{29}$$

We approximate twice the total energy $\int_0^{2\pi} u^2(x,t)dx$ on the discrete level as

$$E = \sum_{i=1}^{I} \frac{1}{2}(u_{i-1}^2 + u_i^2)\Delta x_i. \tag{30}$$

on the grid system in figure 1.

For SCHEME-I in equation (6), the implied discretization of the energy equation is

$$\frac{du_i^2}{dt} + \frac{\widetilde{uu}_{i+1/2} - \widetilde{uu}_{i-1/2}}{(\Delta x_{i+1} + \Delta x_i)/2} = 0 \tag{31}$$

where the tilde "∼" is a special interpolation operator introduced by Morinishi et al. [1]

$$\widetilde{\phi\psi}_{i\pm 1/2} = \frac{1}{2}\phi_{i\pm1}\psi_i + \frac{1}{2}\phi_i\psi_{i\pm1} \tag{32}$$

Combining equations (30) and (31), we obtain

$$\begin{aligned}\frac{dE}{dt} &= \frac{d}{dt}\left[\frac{1}{2}u_0^2\Delta x_1 + \sum_{i=1}^{I-1}\frac{1}{2}(\Delta x_i + \Delta x_{i+1})u_i^2 + \frac{1}{2}u_I^2\Delta x_I\right] \\ &= \left[\frac{1}{2}\Delta x_1\frac{du_0^2}{dt} + \widetilde{uu}_{1/2}\right] - \left[\widetilde{uu}_{I-1/2} - \frac{1}{2}\Delta x_I\frac{du_I^2}{dt}\right],\end{aligned} \tag{33}$$

which mimics the energy-conservation in equation (28), i.e., SCHEME-I conserves energy. For Problem-I, we have dE/dt=0 (or E=const) after applying the periodic BC; for Problem-II, we have $dE/dt \neq 0$ due to the non-periodicity of the numerical solutions.

For SCHEME-II in equation (10), the implied discretization of the energy equation is

$$\frac{du_i^2}{dt} + \left(\frac{2}{\Delta x_{i+1}} - \frac{2}{\Delta x_{i+1} + \Delta x_i}\right)\widetilde{uu}_{i+1/2} + \left(\frac{2}{\Delta x_i} - \frac{2}{\Delta x_{i+1}}\right)u_i^2 + \left(\frac{2}{\Delta x_{i+1} + \Delta x_i} - \frac{2}{\Delta x_i}\right)\widetilde{uu}_{i-1/2} = 0, \tag{34}$$

which is in the similar form to the discretization in equation (10). Combining equations (30) and (34), we have

$$\frac{dE}{dt} = \frac{1}{2}\Delta x_1\frac{du_0^2}{dt} + \sum_{i=1}^{I}\left[(u_{i+1}u_i - u_i^2)/\gamma_i + (u_i^2 - u_iu_{i-1})\gamma_i\right] + \frac{1}{2}\Delta x_I\frac{du_I^2}{dt}, \tag{35}$$

which depends on the numerical solution on all the grid points for arbitrary grids. Hence SCHEME-II in equation (10) is not energy-conservative.

The numerical solution by SCHEME-I in figure 3 oscillates strongly on the grid expanding in the flow direction, and as we show later, the total energy predicted by the scheme grows considerably with time, which seems inconsistent with the energy-conservation of SCHEME-I. This inconsistency is reconciled in Appendix A.

Substituting the Taylor series (8) with $j = 1$ to the discrete energy equation (31) for SCHEME-I, we obtain the modified PDEs for the energy as follows

$$\begin{aligned}\frac{\partial u^2}{\partial t} + \frac{\partial u^2}{\partial x} = &- \frac{1}{2}(\Delta x_{i+1} - \Delta x_i)\frac{\partial^2 u^2}{\partial x^2} + (\Delta x_{i+1} - \Delta x_i)\frac{\partial u}{\partial x}\frac{\partial u}{\partial x} \\ &- \frac{1}{6}\frac{\Delta x_{i+1}^3 + \Delta x_i^3}{\Delta x_{i+1} + \Delta x_i}\left[\frac{\partial^3 u^2}{\partial x^3} - 3\frac{\partial}{\partial x}\left(\frac{\partial u}{\partial x}\frac{\partial u}{\partial x}\right)\right] + O\left(\Delta x^3\right).\end{aligned} \tag{36}$$

We see that the modified PDE for the energy conservation implied by SCHEME-I also has a numerical diffusion term (the first term on the right-hand side of the above equation) which is dissipative or anti-dissipative depending on the local grid stretching. Moreover, SCHEME-I introduces a production or dissipation term for the energy (the second term on the right-hand side of the above equation) which adds energy to or removes energy from the numerical solution consistently. For grids expanding in the flow direction, the term is an energy-production term, and for grids shrinking in the flow direction, it is an energy-dissipation term. Based on this observation, we can see that the numerical solutions by SCHEME-I inherently contain more or less energy than the exact solution simply because of the energy production or dissipation terms introduced by the scheme. The numerical solution by SCHEME-I, however, conserves the total energy E in (30) on the discrete level.

Similarly we can derive the energy conservation implied by SCHEME-II in equation (12) by substituting equation

(8) to (34) as follows

$$\frac{\partial u^2}{\partial t} + \frac{\partial u^2}{\partial x} = -\frac{1}{6}\Delta x_{i+1}\Delta x_i\left[\frac{\partial^3 u^2}{\partial x^3} - 3\frac{\partial}{\partial x}\left(\frac{\partial u}{\partial x}\frac{\partial u}{\partial x}\right)\right] + O\left(\Delta x^3\right). \tag{37}$$

This equation neither has the second-order numerical diffusion term nor has an energy production or dissipation term. Although SCHEME-II does not ensure discrete energy conservation as shown in equation (35), the numerical solution predicted by the scheme may have closer level of total energy than that by SCHEME-I compared to the exact solution. In the following we compare the energy predictions of the different schemes for Problem-I and Problem-II.

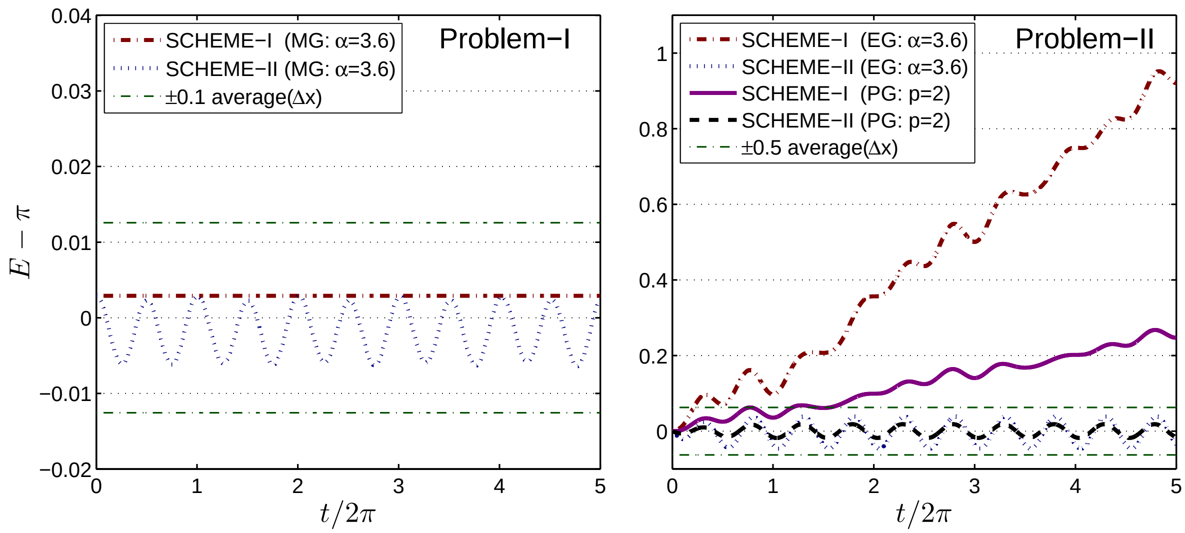

Figure 5: The measurement of the energy-conservation E against time $t/(2\pi)$ with SCHEME-I and SCHEME-II on the EG grid and on the PG grid. The thin dash-dotted lines are reference lines showing the difference from E=π.

The time series of E with the different schemes on the different grids are compared in figure 5. From the left plot of figure 5 for Problem-I with the MG grid, we can see that SCHEME-I yields the energy-conservation. For Problem-I, the energy-conservation requires E=const. The slightly higher value of $E > \pi$ by SCHEME-I shows the difference between the numerical prediction and the exact solution. The predicted value of E by SCHEME-II varies periodically in time, and the time-averaged value of E is slightly less than the exact value E=π. This non-constant value of E confirms that SCHEME-II does not conserve energy exactly. The violation of the energy-conservation by SCHEME-II seems bounded (amplitude of the variations is about 1% of E=π) and does not grow in time for Problem-I.

For Problem-II with the EG and PG grids on the right plot of figure 5, the predicted values of E by SCHEME-I on both grids grow consistently in time as we have mentioned before. The continuously growing energy by SCHEME-I, however, does not violate the energy-conservation on the discrete level. On the discrete level, more energy is added to the numerical solution through the boundaries according to equation (33). The predicted values of E by SCHEME-II on the right plot of figure 5 vary periodically in time and do not grow in time. The amount of energy in Problem-II is captured accurately by SCHEME-II although this scheme is not energy-conservative. From the performance of the two schemes for Problem-II, we observe that, for two comparable schemes (e.g., both second-order accurate), the energy-conservative scheme may be worse in predicting the energy than the non-energy-conservative scheme, which is opposite to intuition.

To summarize, the two central finite-difference schemes on non-uniform grids (SCHEME-I and SCHEME-II) are compared in a linear convection problem in terms of the different numerical properties: accuracy, dissipation, dispersion, momentum-conservation, and energy-conservation. Serious problems are found for the widely used SCHEME-I: amplifying the numerical oscillations and adding energy to the numerical solution for grids expanding in the flow direction, which are dangerous to stable numerical simulations. SCHEME-I conserves momentum and energy on the discrete level although the numerical solutions by SCHEME-I differ from the exact one significantly for certain specified non-uniform grids. SCHEME-II does not conserve momentum and energy on the discrete level in general, but the numerical solutions by SCHEME-II are more accurate than those by SCHEME-I for grids expanding in the flow direction.

In LES, it is often emphasized to use energy-conservative schemes, and many energy-conservative schemes are designed in the literature (e.g., [1, 2, 3, 4]). From the above linear analysis, we can see that the energy-conservative schemes may not be able to yield more accurate numerical solutions simply because the energy-conservative schemes may inherently introduce more energy to the numerical solutions in spite of their energy-conservation on the discrete level. To understand the properties of the schemes thoroughly, in the following, we further evaluate the conservation properties of the two schemes for the simplest non-linear convection problem: the inviscid Burgers' equation.

3. Inviscid Burgers' equation

3.1. Discretization

The inviscid Burgers' equation is

$$\frac{\partial u}{\partial t} + \frac{1}{2}\frac{\partial u^2}{\partial x} = 0, \qquad (0 \leqslant x \leqslant 2\pi,\ 0 \leqslant t \leqslant T). \tag{38}$$

Multiplying the inviscid Burgers' equation with $2u$, we can derive the energy equation as

$$\frac{\partial u^2}{\partial t} + \frac{2}{3}\frac{\partial u^3}{\partial x} = 0, \qquad (0 \leqslant x \leqslant 2\pi,\ 0 \leqslant t \leqslant T). \tag{39}$$

Similar to the analysis in Section 2, we can find that the above equations yield the following conservations

$$\frac{d}{dt}\int_0^{2\pi} u dx = \frac{1}{2}u^2(0,T) - \frac{1}{2}u^2(2\pi,T), \tag{40}$$

$$\frac{d}{dt}\int_0^{2\pi} u^2 dx = \frac{2}{3}u^3(0,T) - \frac{2}{3}u^3(2\pi,T), \tag{41}$$

which require that the numerical schemes mimic these conservations on the discrete level.

Using SCHEME-I in equation (4) to the inviscid Burgers' equation (38) on the grids shown in figure 1, we have

$$\frac{du_i}{dt} + \frac{u^2_{i+1/2} - u^2_{i-1/2}}{\Delta x_i + \Delta x_{i+1}} = 0, \tag{42}$$

where the cell center values $u_{i\pm 1/2}$ can be obtained from the linear interpolation in equation (5). We denote the scheme in equation (42) as SCHEME-IA. Combining equations (24) and (42), we obtain

$$\frac{dC}{dt} = \left[\frac{1}{2}\Delta x_1 \frac{du_0}{dt} + \frac{1}{2}u^2_{1/2}\right] - \left[\frac{1}{2}u^2_{I-1/2} - \frac{1}{2}\Delta x_I \frac{du_I}{dt}\right], \tag{43}$$

so SCHEME-IA conserves momentum. From equation (42), we can derive the implied energy discrete equation as

$$\frac{du_i^2}{dt} + \frac{\widetilde{uu^2}_{i+1/2} - \widetilde{uu^2}_{i-1/2}}{\Delta x_i + \Delta x_{i+1}} + u_i \left[\frac{\widetilde{uu}_{i+1/2} - \widetilde{uu}_{i-1/2}}{2(\Delta x_i + \Delta x_{i+1})} \right] = 0. \tag{44}$$

Using equations (30) and (44), we obtain

$$\frac{dE}{dt} = \left[\frac{1}{2}\Delta x_1 \frac{du_0^2}{dt} + \frac{1}{2}\widetilde{uu^2}_{1/2} \right] - \left[\frac{1}{2}\widetilde{uu^2}_{I-1/2} - \frac{1}{2}\Delta x_I \frac{du_I^2}{dt} \right] - \sum_{i=1}^{I-1} \frac{1}{4} u_i \left(\widetilde{uu}_{i+1/2} - \widetilde{uu}_{i-1/2} \right). \tag{45}$$

The righthand side of equation (45) depends on the numerical solutions on all the grid points, so SCHEME-IA is not energy-conservative.

An energy-conservative discretization of the inviscid Burgers' equation (38) is found in the following

$$\frac{du_i}{dt} + \frac{1}{3}\left[\frac{\widetilde{uu}_{i+1/2} - \widetilde{uu}_{i-1/2}}{\Delta x_i + \Delta x_{i+1}} \right] + \frac{2}{3}\left[\frac{u_{i+1}^2 - u_{i-1}^2}{2(\Delta x_i + \Delta x_{i+1})} \right] = 0. \tag{46}$$

which is obtained by splitting the spatial derivative in equation (38) into two parts and using the two different discretizations (the second and the third term in the above equation) to approximate each part. We denote this scheme as SCHEME-IB. Combining equations (24) and (46), we obtain

$$\frac{dC}{dt} = \left[\frac{1}{2}\Delta x_1 \frac{du_0}{dt} + \frac{1}{6}\widetilde{uu}_{1/2} + \frac{1}{6}u_0^2 + \frac{1}{6}u_1^2 \right] - \left[\frac{1}{6}\widetilde{uu}_{I-1/2} + \frac{1}{6}u_I^2 + \frac{1}{6}u_{I+1}^2 - \frac{1}{2}\Delta x_I \frac{du_I}{dt} \right], \tag{47}$$

so SCHEME-IB is momentum-conservative. From equation (46), we can derive the implied energy discrete equation as

$$\frac{du_i^2}{dt} + \frac{2}{3}\left[\frac{\widetilde{uu^2}_{i+1/2} - \widetilde{uu^2}_{i-1/2}}{(\Delta x_i + \Delta x_{i+1})/2} \right] = 0. \tag{48}$$

Using equations (30) and (48), we obtain

$$\frac{dE}{dt} = \left[\frac{1}{2}\Delta x_1 \frac{du_0^2}{dt} + \frac{2}{3}\widetilde{uu^2}_{1/2} \right] - \left[\frac{2}{3}\widetilde{uu^2}_{I-1/2} - \frac{1}{2}\Delta x_I \frac{du_I^2}{dt} \right], \tag{49}$$

so SCHEME-IB is energy-conservative.

Using SCHEME-II in equation (9) to the inviscid Burgers' equation (38), we have

$$\frac{du_i}{dt} + \left(\frac{1}{\Delta x_{i+1}} - \frac{1}{\Delta x_{i+1} + \Delta x_i} \right) u_{i+1/2}^2 + \left(\frac{1}{\Delta x_i} - \frac{1}{\Delta x_{i+1}} \right) u_i^2 + \left(\frac{1}{\Delta x_{i+1} + \Delta x_i} - \frac{1}{\Delta x_i} \right) u_{i-1/2}^2 = 0, \tag{50}$$

from which, we can derive the discrete energy equation as

$$\begin{aligned} \frac{du_i^2}{dt} &+ \left[\left(\frac{1}{\Delta x_{i+1}} - \frac{1}{\Delta x_{i+1} + \Delta x_i} \right) \widetilde{uu^2}_{i+1/2} + \left(\frac{1}{\Delta x_i} - \frac{1}{\Delta x_{i+1}} \right) u_i^3 + \left(\frac{1}{\Delta x_{i+1} + \Delta x_i} - \frac{1}{\Delta x_i} \right) \widetilde{uu^2}_{i-1/2} \right] \\ &+ \frac{1}{2}u_i^2 \left[\left(\frac{1}{\Delta x_{i+1}} - \frac{1}{\Delta x_{i+1} + \Delta x_i} \right) u_{i+1} + \left(\frac{1}{\Delta x_i} - \frac{1}{\Delta x_{i+1}} \right) u_i + \left(\frac{1}{\Delta x_{i+1} + \Delta x_i} - \frac{1}{\Delta x_i} \right) u_{i-1} \right] = 0. \end{aligned} \tag{51}$$

We can demonstrate that SCHEME-II for the inviscid Burgers' equation is neither momentum-conservative nor energy-conservative.

There are many variants of using the central difference schemes on the inviscid Burgers' equation, we limit our discussion on the above three schemes: SCHEME-IA in (42), SCHEME-IB in (46), and SCHEME-II in (50).

We can do the same analysis as in Section 2 by using the modified PDEs for the above three schemes to understand these schemes thoroughly. The modified PDE for SCHEME-IA in equation (42) can be derived as

$$\begin{aligned}\frac{\partial u}{\partial t}+\frac{1}{2}\frac{\partial u^2}{\partial x} = & -\frac{1}{2}\left(\Delta x_{i+1}-\Delta x_i\right)\frac{\partial}{\partial x}\left(u\frac{\partial u}{\partial x}\right)+\frac{1}{4}\left(\Delta x_{i+1}-\Delta x_i\right)\frac{\partial u}{\partial x}\frac{\partial u}{\partial x}\\ & -\frac{1}{2}\frac{\Delta x_{i+1}^3+\Delta x_i^3}{\Delta x_{i+1}+\Delta x_i}\left[\frac{1}{3}\frac{\partial}{\partial x}\left(u\frac{\partial^2 u}{\partial x^2}\right)+\frac{1}{12}\frac{\partial}{\partial x}\left(\frac{\partial u}{\partial x}\frac{\partial u}{\partial x}\right)\right]+O(\Delta x^3).\end{aligned} \tag{52}$$

The truncation errors resulted from SCHEME-IA for the inviscid Burgers' equation have similar properties as those for the linear convection problem in equation (11). The first term on the righthand side of equation (52) is a numerical diffusion term which is dissipative on grids shrinking in the flow direction ($(\Delta x_{i+1}-\Delta x_i)u<0$) and anti-dissipative on grids expanding in the flow direction ($(\Delta x_{i+1}-\Delta x_i)u>0$). Moreover, SCHEME-IA introduces a source or sink for the momentum (the second term on the righthand side of equation (52)). Whether it is a source or sink solely depends on the local grid stretching independent of the flow fields, i.e., it is a source (the term is non-negative) if $(\Delta x_{i+1}-\Delta x_i)>0$ and a sink (the term is non-positive) if $(\Delta x_{i+1}-\Delta x_i)<0$. The third term on the righthand side of equation (52) is the dispersion error.

The modified PDE for SCHEME-IB in equation (46) is

$$\begin{aligned}\frac{\partial u}{\partial t}+\frac{1}{2}\frac{\partial u^2}{\partial x} = & -\frac{1}{2}\left(\Delta x_{i+1}-\Delta x_i\right)\frac{\partial}{\partial x}\left(u\frac{\partial u}{\partial x}\right)+\frac{1}{6}\left(\Delta x_{i+1}-\Delta x_i\right)\frac{\partial u}{\partial x}\frac{\partial u}{\partial x}\\ & -\frac{1}{6}\frac{\Delta x_{i+1}^3+\Delta x_i^3}{\Delta x_{i+1}+\Delta x_i}\left[\frac{\partial}{\partial x}\left(u\frac{\partial^2 u}{\partial x^2}\right)+\frac{1}{2}\frac{\partial}{\partial x}\left(\frac{\partial u}{\partial x}\frac{\partial u}{\partial x}\right)\right]+O(\Delta x^3).\end{aligned} \tag{53}$$

which has the same form of the truncation error terms on the righthand side as equation (52) except the difference in the constant coefficient of the terms, e.g., the source or sink term in (53) has smaller constant coefficient $1/6$ than $1/4$ in (52).

The modified PDE for SCHEME-II in equation (50) is

$$\frac{\partial u}{\partial t}+\frac{1}{2}\frac{\partial u^2}{\partial x}=-\frac{1}{2}\Delta x_i\Delta x_{i+1}\left[\frac{1}{3}\frac{\partial}{\partial x}\left(u\frac{\partial^2 u}{\partial x^2}\right)+\frac{1}{12}\frac{\partial}{\partial x}\left(\frac{\partial u}{\partial x}\frac{\partial u}{\partial x}\right)\right]+O(\Delta x^3). \tag{54}$$

which does not have the second-order numerical diffusion term and the source or sink term on the righthand side. This shows the numerical superiority of SCHEME-II over SCHEME-IA and SCHEME-IB although SCHEME-II does not conserve momentum on the discrete level.

We can also derive the modified PDEs for the discrete energy equations (44), (48), and (51). For SCHEME-IA and SCHEME-IB, the modified PDEs for the discrete energy equations are

$$\begin{aligned}\frac{\partial u^2}{\partial t}+\frac{2}{3}\frac{\partial u^3}{\partial x} = & -\frac{1}{2}\left(\Delta x_{i+1}-\Delta x_i\right)\frac{\partial}{\partial x}\left(u\frac{\partial u^2}{\partial x}\right)+\frac{3}{2}\left(\Delta x_{i+1}-\Delta x_i\right)u\frac{\partial u}{\partial x}\frac{\partial u}{\partial x}\\ & -\frac{1}{2}\frac{\Delta x_{i+1}^3+\Delta x_i^3}{\Delta x_{i+1}+\Delta x_i}\left[\frac{\partial}{\partial x}\left(\frac{2}{3}u^2\frac{\partial^2 u}{\partial x^2}-\frac{1}{6}u\frac{\partial u}{\partial x}\frac{\partial u}{\partial x}\right)+\frac{1}{6}\left(\frac{\partial u}{\partial x}\right)^3\right]+O(\Delta x^3),\end{aligned} \tag{55}$$

and

$$\frac{\partial u^2}{\partial t} + \frac{2}{3}\frac{\partial u^3}{\partial x} = - \frac{1}{2}\left(\Delta x_{i+1} - \Delta x_i\right)\frac{\partial}{\partial x}\left(u\frac{\partial u^2}{\partial x}\right) + \frac{4}{3}\left(\Delta x_{i+1} - \Delta x_i\right)u\frac{\partial u}{\partial x}\frac{\partial u}{\partial x} - \frac{1}{3}\frac{\Delta x_{i+1}^3 + \Delta x_i^3}{\Delta x_{i+1} + \Delta x_i}\frac{\partial}{\partial x}\left(u^2\frac{\partial^2 u}{\partial x^2}\right) + O(\Delta x^3). \tag{56}$$

Both modified PDEs (55) and (56) are in the same form except the slight difference in the constant coefficients. The first terms on the righthand sides of equations (55) and (56) are the numerical diffusion terms which have the same dissipation property as in (52) and (53). The second terms on the righthand side of equations (55) and (56) are the energy production or dissipation which depends on the local grid stretching and the flow direction. On grids expanding in the flow direction ($(\Delta x_{i+1} - \Delta x_i)u > 0$), it is energy-production (the term is non-negative), and on grids shrinking in the flow direction ($(\Delta x_{i+1} - \Delta x_i)u < 0$), it is energy-dissipation (the term is non-positive). The energy production or dissipation term for SCHEME-IB has slightly lower magnitude ($4/3$) than that for SCHEME-IA ($3/2$). The third terms on the righthand side of equations (55) and (56) are the numerical dispersion terms.

The modified PDE for the discrete energy equation (57) of SCHEME-II is

$$\frac{\partial u^2}{\partial t} + \frac{2}{3}\frac{\partial u^3}{\partial x} = -\frac{1}{2}\Delta x_i \Delta x_{i+1}\left[\frac{\partial}{\partial x}\left(\frac{2}{3}u^2\frac{\partial^2 u}{\partial x^2} - \frac{1}{6}u\frac{\partial u}{\partial x}\frac{\partial u}{\partial x}\right) + \frac{1}{6}\left(\frac{\partial u}{\partial x}\right)^3\right] + O(\Delta x^3), \tag{57}$$

which does not have the numerical diffusion term and the energy production or dissipation term. Although SCHEME-II is not energy-conservative, SCHEME-II is superior to SCHEME-IB due to its free of energy production or dissipation in the modified PDEs.

To sum up, in the above conservation analysis, we observe the following conservation properties for the different schemes: SCHEME-IA is momentum-conservative but not energy-conservative, SCHEME-IB is momentum-conservative and energy-conservative, and SCHEME-II is neither momentum-conservative nor energy-conservative. From the analysis based on the modified PDEs, we observe that SCHEME-IA and SCHEME-IB introduce the numerical diffusion and the source or sink to the momentum, and the numerical diffusion and production or dissipation to the energy, while SCHEME-II is free of the numerical diffusion, the momentum source or sink, and the energy production or dissipation. In the following, we perform numerical tests to evaluate these different numerical properties of the different schemes for the inviscid Burgers' equation on a periodic test case and a non-periodic test case.

3.2. Periodic test case

The inviscid Burgers' equation (38) is numerically solved on domain $[0, 2\pi]$ starting from the following initial condition to the stopping time $T = 20\pi$,

$$u(x, 0) = \frac{\exp(-x) - \exp(-2\pi)}{1 - \exp(-2\pi)} + \frac{\tanh\left(10(x - \pi)\right) + 1}{2} + 1. \tag{58}$$

The MG grid with $\alpha = 3.6$ in equation (14) is used with the number of grid cells $I = 50$. The periodic BC $u(0, t) = u(2\pi, t)$ is applied during the time advancement. The Crank-Nicholson scheme is used for the time integration.

With the periodic BC, we can find that dC/dt=0 (C=const) from equation (43) for SCHEME-IA and from equation (47) for SCHEME-IB, and dE/dt=0 (E=const) from equation (49) for SCHEME-IB.

The time series of the momentum-conservation C and energy-conservation E for the different schemes are shown in figure 6. From the left plot of figure 6, we can see that the values of C remain constant all the time for SCHEME-

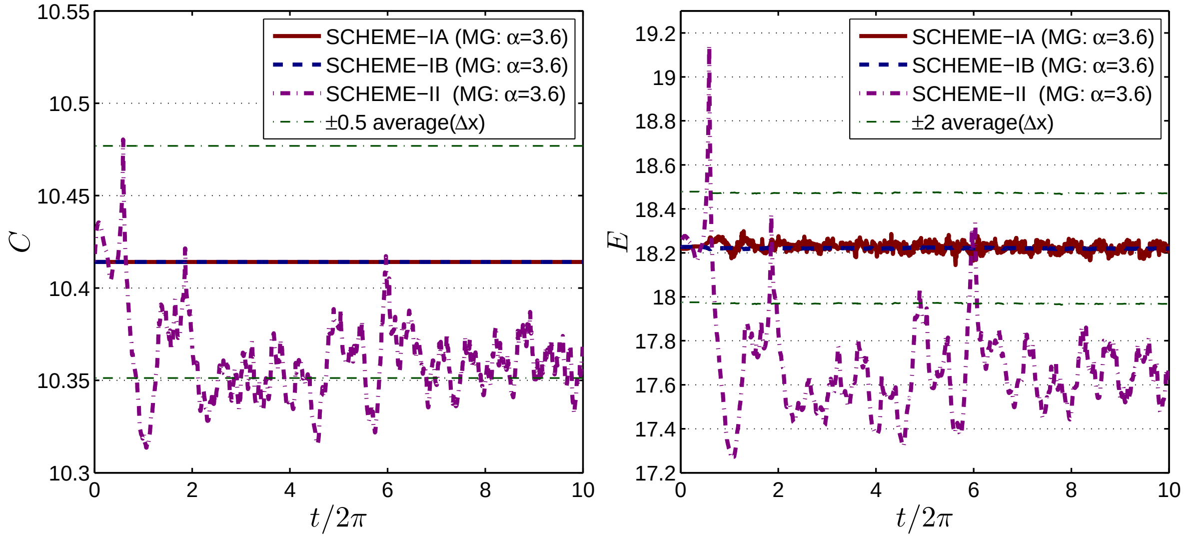

Figure 6: The measurement of the momentum-conservation C and the energy-conservation E against time $t/(2\pi)$ with SCHEME-IA, SCHEME-IB and SCHEME-II on the MG grid for the periodic test case. (The thin dash-dotted lines are reference lines showing the difference from the values of C and E by SCHEME-IB.)

IA and SCHEME-IB due to the fact that these schemes are momentum-conservative. (The solid and dashed lines overlap on the left plot of figure 6.) The values of C by SCHEME-II vary with time, which is consistent with the non-momentum-conservative property of the scheme. After about $t/2\pi = 1$, the values of C by SCHEME-II fluctuate around the value of 10.35, about 1% lower than the values of C by SCHEME-IA and SCHEME-IB. The violation of momentum-conservation by SCHEME-II does not seem to be growing with time. From the right plot of figure 6, we can see that only the values of E from SCHEME-IB remain constant all the time because only SCHEME-IB is energy-conservative and the other two schemes are not. Comparing the two non-energy-conservative schemes in the figure, SCHEME-IA seems better than SCHEME-II in terms of energy-conservation because the magnitude of the variations in E by SCHEME-IA is smaller that by SCHEME-II. After about $t/2\pi = 1$, the values of E by SCHEME-II fluctuate around the value of 17.6, about 3% lower than the value of E by SCHEME-IB. The violation of energy-conservation by SCHEME-IA and SCHEME-II do not grow with time. These results are consistent with the conservation analysis based on the discrete equations, and hence confirm that analysis.

In sum, in figure 6, we examined the conservation of the numerical solutions by the different schemes, in which we have not examined the detailed numerical solutions (e.g., how close the numerical solutions are to the exact one?). In the following, we consider a non-periodic test case, in which we explore and compare the accuracy of the numerical solutions in addition to the conservation.

3.3. Non-periodic test case

We consider the following initial condition for the numerical solution of the inviscid Burgers' equation (38) on domain $[0, 2\pi]$,

$$u(x,0) = \frac{1}{\exp(x - 3/20)[\tanh(10x-3)+1] - \tanh(10x-3) + 1} \tag{59}$$

with the boundary conditions: $u(0,t)$=$u(0,0)$≈0.5002 and $\partial u(x,t)/\partial x|_{x=2\pi} = 0$. The Neumann BC on the right side is introduced numerically for the treatment of the right boundary for the central-difference schemes although only one BC is allowed mathematically. The numerical solutions are advanced to the stopping time $T = 40\pi$, at which the steady state solution $u(x,T) = u(0,T)$ is expected. The EG grid with $\alpha = 3.6$ in equation (14) is used with the number of grid cells $I = 50$.

The time evolution of the numerical solutions for the non-periodic problem with the three schemes are shown in figure 7 at the selected times $t/2\pi$=0, 0.1, 0.25, 0.5, 1, 2, 6, and 16. The x-axis is shown in the log-scale to examine the regions where the grid spacing is fine. The thin lines with symbols are the numerical results from the three schemes. The thick lines (without symbols) are high-resolution numerical solutions computed by the first-order upwind scheme. These high-resolution numerical results serve as “exact” solution for the comparison. The initial condition is smooth and shows decaying in the flow direction, which is to mimic the centerline velocity decay in jet flows. The convection is toward the right. The difference of the convecting velocity on the left and right eventually causes a sharp interface as shown at about $t/2\pi = 1$ in the figure. The sharp interface ultimately is convected out of the domain, and a steady state solution $u(x,\infty) = u(0,\infty)$ is expected as indicated by the “exact” solution. All three schemes perform similarly before $t/2\pi = 0.25$. After that, strong oscillations behind the sharp interface are observed due to the dispersive nature of all three schemes. The schemes behave qualitatively different upstream ($x < 1$). SCHEME-IA and SCHEME-IB produce strong oscillations upstream, while SCHEME-II preserves the upcoming constant value very well. This can be explained by the anti-dissipative property of SCHEME-IA and SCHEME-IB on the given grids. The numerical oscillations (produced by the numerical dispersion) are amplified by the negative numerical diffusion in equations (52) and (53). In contrast, SCHEME-II is dissipation-free, so the numerical oscillations caused by the numerical dispersion upstream (not visible in figure 7) are not amplified. At the final time $t/2\pi = 16$ in figure 7, the results by SCHEME-II reaches the steady state solution which agrees with the “exact” solution well. The results by SCHEME-IA still contain numerical oscillations, especially for the first five grid points. The results by SCHEME-IB are improved compared to those by SCHEME-IA probably because the energy-production term by SCHEME-IB in equation (56) is smaller in magnitude than that by SCHEME-IA in equation (55) although the first three grid points still show strong oscillation. For this simple non-linear convection, we show that the energy-conservative scheme (SCHEME-IB) performs worse than the non-energy-conservative scheme (SCHEME-II). The effect of the schemes upstream is very informative to the discussion of the LES simulations of jet flows in the following sections.

Figure 8 shows the time series of the values of C and E for the non-periodic test case with the different schemes. The values of C and E increase from the initial value and approach constants after some time. The detailed evolutions of C and E are different for the three schemes. For SCHEME-II (dash-dotted lines in figure 8), the values of C and E increase initially, and, at about $t/2\pi = 3.5$, they quickly become flat. During the transition, the total energy E by SCHEME-II does not exceed the final steady-state energy, which indicates good numerical stability. The predictions of E by SCHEME-II agree with the “exact” solution very well. For SCHEME-IA (solid lines in figure 8), the values of C increase initially, and become flat at about the same time $t/2\pi = 3.5$. But the values of C fluctuate even after a long time ($t/2\pi = 20$) and do not seem to become steady. And the time-averaged value of C at the steady state stage predicted by SCHEME-IA is slightly lower than the “exact” value. The energy E by SCHEME-IA is always higher than the “exact” one in the right plot of figure 8 due to the energy production caused by SCHEME-IA in (55) for the test case. The values of E by SCHEME-IA do not seem to become steady after a long time neither. For SCHEME-IB (dashed lines in figure 8), both values of C and E increase initially and overshoot at about $t/2\pi = 5.3$. Then they reduces asymptotically to some constant values. This overshoot of the total energy can be explained by the energy

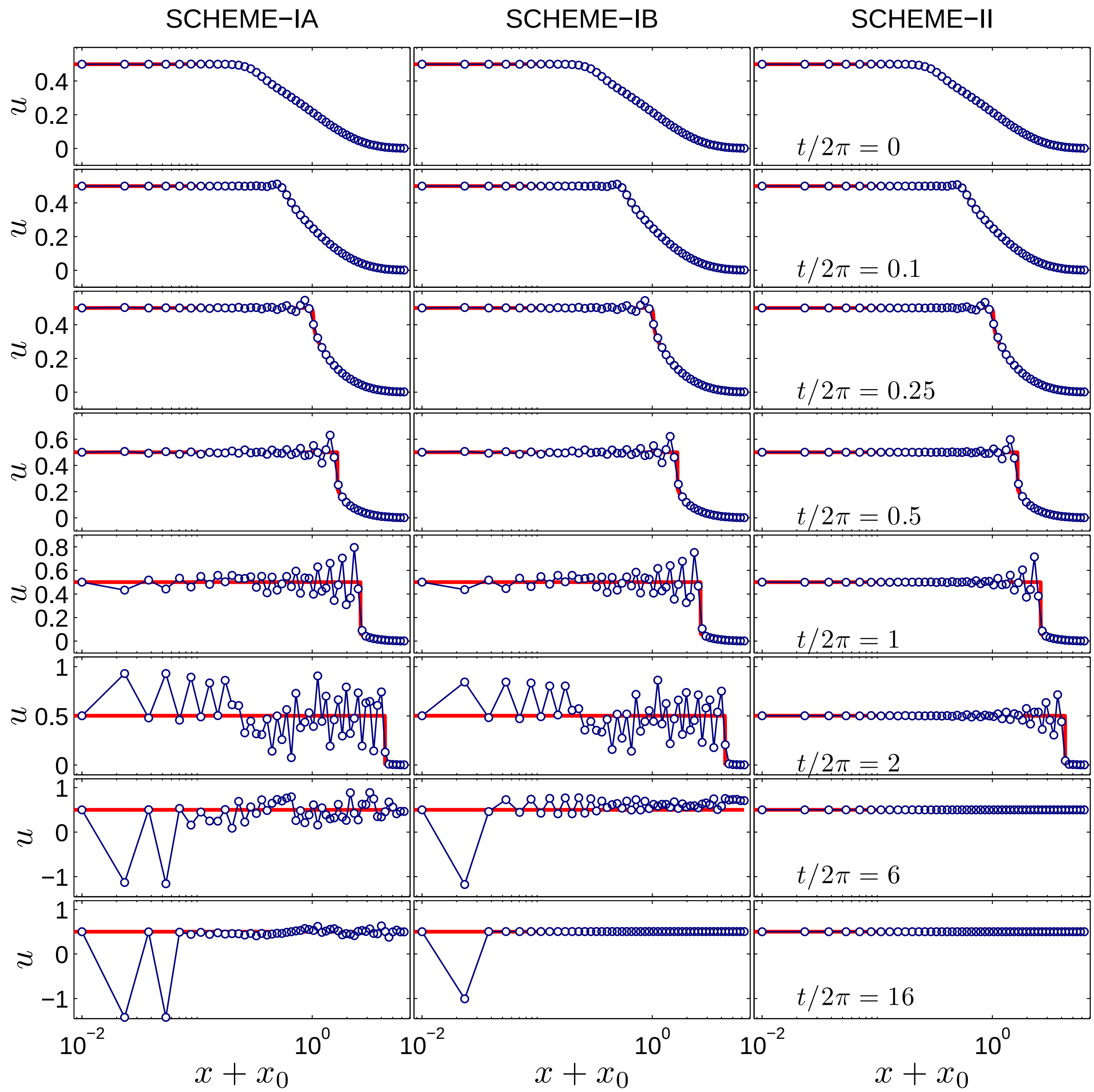

Figure 7: The time evolution of the numerical solutions for the non-periodic problem with SCHEME-IA, SCHEME-IB, and SCHEME-II at the selected times $t/2\pi$=0, 0.1, 0.25, 0.5, 1, 2, 6, and 16. The thin solid lines with symbols are the numerical results from the three schemes. The thick solid lines are high-resolution numerical solutions from the first-order upwind scheme. (The x-axis is shifted by $x_0 = 0.01$ so that the first grid point $x = 0$ can be shown in the log scale of the x-axis.)

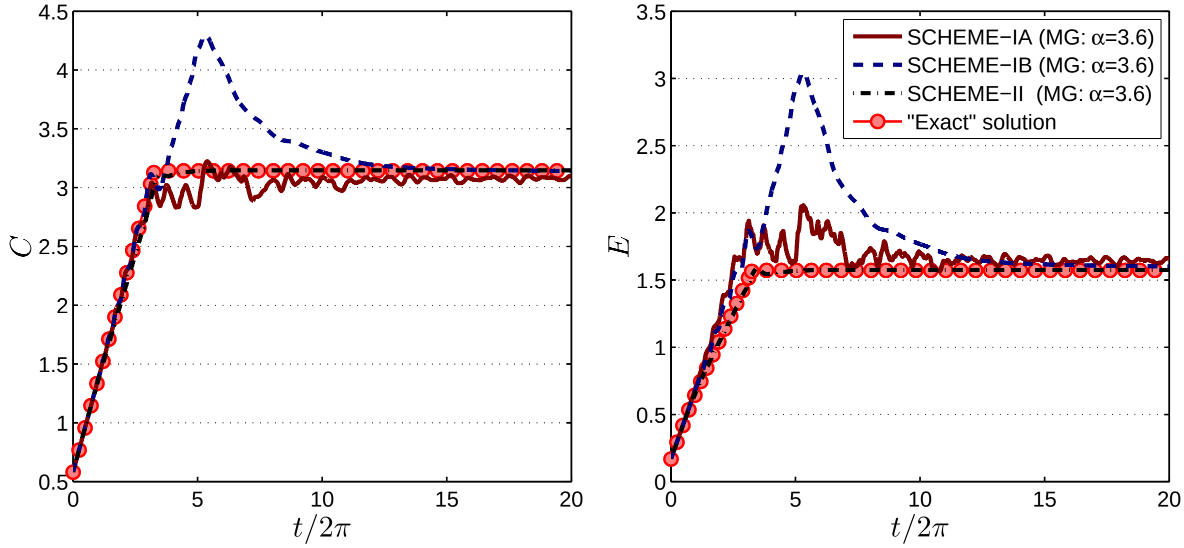

Figure 8: The measurement of the conservation C and the energy conservation E for the non-periodic problem against time $t/(2\pi)$ with SCHEME-IA, SCHEME-IB and SCHEME-II on the exponential grids (EG). The “exact” solution is from a high-resolution numerical simulation by the first-order upwind scheme.

production in (55) too. The maximum energy E by both SCHEME-IA and SCHEME-IB during the transition exceeds the final “exact” value, which indicates that they are less stable than SCHEME-II. The generated energy by SCHEME-IA and SCHEME-IB degenerates the numerical accuracy and may cause serious instability in more complicated LES calculations.

In the following, we compare SCHEME-I and SCHEME-II in the practical LES of turbulent flows which is more complicated, to further show the deficiency of SCHEME-I and the superiority of SCHEME-II.

4. Large eddy simulations (LES)

The LES methods used in this study are outlined in this Section. A laminar jet flow test case is performed first to compare the performance of SCHEME-I and SCHEME-II in this relatively simple problem. More complicated LES studies are performed in the following Sections 5 and 6.

4.1. Numerical methods

The numerical methods for LES used in this study are based on [14, 20]. The basics of the numerical methods are summarized here. For details, the reader is referred to [14, 20, 26, 33, 34].

Applying the traditional filtering operation to the mass, momentum, and scalar conservation equations, we can derive the LES equations. After modeling for the terms accounting for the sub-filter stresses and sub-filter scalar fluxes, the closed set of LES equations to solve for low Mach number flows is the following

$$\frac{\partial \overline{\rho}}{\partial t} + \nabla \cdot (\overline{\rho}\,\widetilde{\mathbf{u}}) = 0, \tag{60}$$

$$\frac{\partial \overline{\rho}\,\widetilde{\mathbf{u}}}{\partial t} + \nabla \cdot (\overline{\rho}\,\widetilde{\mathbf{u}}\,\widetilde{\mathbf{u}}) = \nabla \cdot [2(\mu + \mu_t)\mathbf{S}] - \nabla \overline{p}, \tag{61}$$

$$\mathbf{S} = 1/2\left[\nabla \widetilde{\mathbf{u}} + (\nabla \widetilde{\mathbf{u}})^{\mathrm{T}}\right] - 1/3\,\delta \nabla \cdot \widetilde{\mathbf{u}}, \tag{62}$$

$$
\begin{aligned}
\frac{\partial\overline{\rho}\widetilde{\xi}}{\partial t} + \nabla\cdot\left(\overline{\rho}\,\widetilde{\mathbf{u}}\,\widetilde{\xi}\right) &= \nabla\cdot\left[\overline{\rho}(\Gamma+\Gamma_t)\nabla\widetilde{\xi}\right], && (63)\\
\frac{\partial\overline{\rho}\widetilde{\xi^2}}{\partial t} + \nabla\cdot\left(\overline{\rho}\,\widetilde{\mathbf{u}}\,\widetilde{\xi^2}\right) &= \nabla\cdot\left[\overline{\rho}(\Gamma+\Gamma_t)\nabla\widetilde{\xi^2}\right] - \widetilde{\chi}, && (64)\\
\overline{\rho} &= f\left(\widetilde{\xi},\widetilde{\xi^2}\right). && (65)
\end{aligned}
$$

Here the bar "–" and tilde "∼" denote filtering and density-weighted filtering, respectively. The variable $\overline{\rho}$ denotes the filtered density, $\widetilde{\mathbf{u}}$ the filtered velocity vector, $\overline{p}$ the filtered pressure, μ the dynamic viscosity, μ_t the sub-filter eddy viscosity, $\boldsymbol{\delta}$ the unit tensor, $\widetilde{\xi}$ the filtered mixture fraction, $\widetilde{\xi^2}$ the filtered mixture fraction squared, Γ the molecular diffusivity, Γ_t the sub-filter eddy diffusivity, $\widetilde{\chi}$ the sub-filter dissipation rate of the mixture fraction. The sub-filter eddy viscosity μ_t, eddy diffusivity Γ_t and dissipation rate $\widetilde{\chi}$ are modeled as

$$
\begin{aligned}
\mu_t &= C_\mu\overline{\rho}\Delta^2|\mathbf{S}|, && (66)\\
\Gamma_t &= C_\Gamma\Delta^2|\mathbf{S}|, && (67)\\
|\mathbf{S}| &= \left(S_{ij}S_{ij}\right)^{1/2} && (68)\\
S_{ij} &= \frac{1}{2}\left(\frac{\partial u_i}{\partial x_j}+\frac{\partial u_j}{\partial x_i}\right) - \frac{1}{3}\delta_{ij}\frac{\partial u_k}{\partial x_k} && (69)
\end{aligned}
$$

where Δ is the filter width, δ_{ij} is Kronecker delta, and the model coefficients C_μ and C_Γ are computed by the Dynamic Model [14, 20].

For constant-density flows, equations (60)-(62) form a closed set of equations. The additional equations (63)-(65) are for variable-density flows with equation (65) being the state equation to obtain density. A simple flamelet model [34] is used in this work to model the density coupling.

The LES equations in the above are cast in the cylindrical coordinates, and are discretized with the second-order central-difference schemes for the spatial derivatives and the Crank-Nicolson scheme for the time advancement. A staggered grid system in both space and time is used for the discretization. The QUICK scheme [14] is used for the convection terms in the mixture fraction equations (63) and (64) to reduce the excessive numerical oscillations near the upper and lower bounds of the mixture fraction [14]. For the discretization of the staggered velocity, we face the same problem discussed in Section 2 when using central-difference schemes which will be discussed in detail in the following Section 4.2. The pressure projection (or fractional-step method) is used to enforce continuity. An iterative semi-implicit scheme is employed to solve the coupled non-linear equations. The time-step size Δt is controlled by the maximum allowed CFL number, $\text{CFL} = |\tilde{u}|\Delta t/\Delta x + 4(\mu+\mu_t)\Delta t/\overline{\rho}\Delta x^2 \leqslant \text{CFL}_{\max}$, where the CFL number is defined only on the quantities in the axial direction, since the explicit treatment is in the axial direction only during the iteration employed in the current numerical methods. For more numerical details, please refer to [14, 20].

4.2. Discretization of convection terms

When discretizing the non-linear convection terms such as $\partial(\overline{\rho}\tilde{u}\tilde{u})/\partial x$, $\partial(\overline{\rho}\tilde{v}\tilde{v})/\partial y$ and $\partial(\overline{\rho}\tilde{w}\tilde{w})/\partial z$ in the momentum equation (61) on the staggered non-uniform grids, we face the same situation of choosing SCHEME-I or SCHEME-II as discussed in Section 2. In the past, SCHEME-I has been used dominantly for discretizing these convection terms for LES studies.

We take the discretization of $\partial(\overline{\rho}\tilde{u}\tilde{u})/\partial x$ as an example in the following discussion, and the other terms can be discretized similarly. The convection terms are discretized on a non-uniform grid system shown in figure 9. The

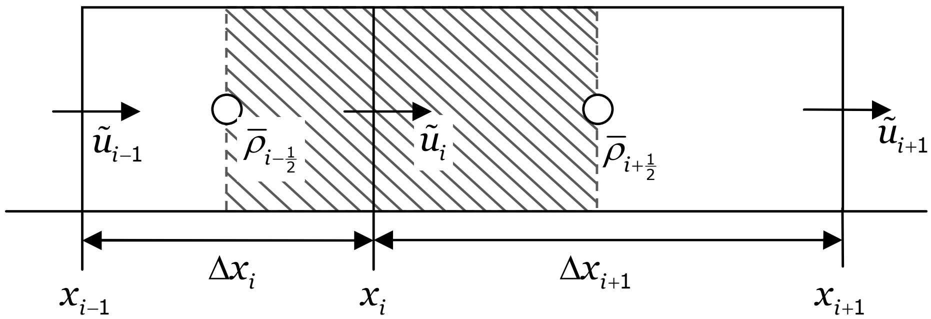

Figure 9: The staggered grid system for the large eddy simulations.

scalars (such as $\overline{\rho}$, $\overline{p}$, $\tilde{\xi}$) are stored at the cell centers indicated by the circles in the figure, and the velocity component $\tilde{u}$ is located at the cell faces x_i.

We rewrite $\overline{\rho}\tilde{u}\tilde{u}$ as $g\tilde{u}$ where $g = \overline{\rho}\tilde{u}$ is the mass flux. The mass flux g is also stored at the cell face x_i to have a natural mass conservation over the grid cell, and is computed from $\overline{\rho}$ and $\tilde{u}$ with necessary linear interpolation.

With SCHEME-I, the convection $\partial(\overline{\rho}\tilde{u}\tilde{u})/\partial x$ is discretized as

$$\left(\frac{\partial g\tilde{u}}{\partial x}\right)_i = \frac{g_{i+1/2}\tilde{u}_{i+1/2} - g_{i-1/2}\tilde{u}_{i-1/2}}{1/2(\Delta x_{i+1} + \Delta x_i)}. \tag{70}$$

This central-difference scheme is the same as the finite-volume scheme over the control volume $[x_{i-1/2}, x_{i+1/2}]$ shown in figure 9. The unknown quantities in equation (70) are interpolated from the nearest known values with the linear interpolation in equation (5), e.g., $\tilde{u}_{i+1/2} = 1/2(\tilde{u}_{i+1} + \tilde{u}_i)$.

With SCHEME-II, we discretize the convection $\partial(\overline{\rho}\tilde{u}\tilde{u})/\partial x$ as

$$\left(\frac{\partial g\tilde{u}}{\partial x}\right)_i = \left(\frac{2}{\Delta x_{i+1}} - \frac{2}{\Delta x_{i+1} + \Delta x_i}\right) g_{i+1/2}\tilde{u}_{i+1/2} + \left(\frac{2}{\Delta x_i} - \frac{2}{\Delta x_{i+1}}\right) g_i\tilde{u}_i + \left(\frac{2}{\Delta x_{i+1} + \Delta x_i} - \frac{2}{\Delta x_i}\right) g_{i-1/2}\tilde{u}_{i-1/2}. \tag{71}$$

The unknown quantities are interpolated from the nearest known values.

The numerical properties of SCHEME-I and SCHEME-II have been discussed comprehensively in Sections 2 and 3. In the following we compare these schemes in equations (70) and (71) in the practical LES of several test cases. We perform the simulations for a laminar flow first. Then we compare the schemes in the LES of turbulent jet flows with and without density variations which exhibit strong variations of turbulence fields in the three-dimensional space and time.

4.3. Test case: constant-density laminar jet with Re=300

A constant-density laminar jet issuing into quiescent environment is simulated with Reynolds number $Re = 300$. The computational domain in the axial and the radial directions is $[0, 40D] \times [0, 10D]$ where D is the jet diameter. A number of $64 \times 64 \times 16$ grid cells are used in the axial, radial and azimuthal directions, respectively. In the axial direction, the grid spacing is stretched in the axial direction, which yields the smallest grid spacing at the jet inlet and the largest grid spacing at the outflow plane, and the ratio about 11.4 of the largest and smallest grid sizes. In the radial direction, the grid spacing is clustered near the axis and the jet pipe. A uniform grid is used in the azimuthal direction. Fully developed laminar pipe flow is used for the jet inlet condition, and the convective boundary condition [14, 20] is used on the lateral and outflow boundaries. The sub-filter models are disabled by setting $C_\mu = 0$ in equation

(66) for the laminar simulation. SCHEME-II is implemented in a code originally developed in [14] and is compared to SCHEME-I that was used in the original code. For reference, a uniform grid in the axial direction is also used, in which case SCHEME-I and SCHEME-II are identical. The time-step size is controlled by $CFL_{max} = 0.5$ for the time advancement.

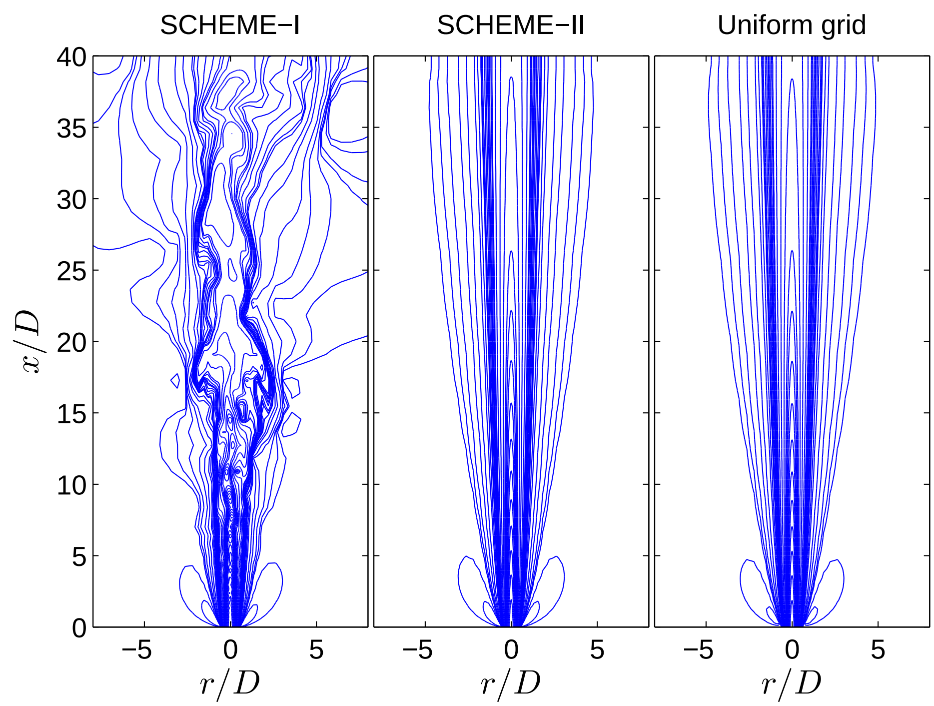

Figure 10: Contour plots of the axial velocity u in the laminar jet flow with non-uniform axial grid (SCHEME-I and SCHEME-II) and with uniform axial grid.

In figure 10, the contours of the axial velocity u in a x-r plane are compared with the different schemes and the different grids. SCHEME-I on the non-uniform grid generates significant fluctuations of the axial velocity (left plot in figure 10). The strong fluctuations in the results by SCHEME-I are non-physical, and are caused by the numerical errors. SCHEME-II on the non-uniform grid produces smooth numerical solutions (middle plot in figure 10), so does the scheme on uniform grids (right plot in figure 10). The axial profiles of the centerline velocity are further compared in figure 11. SCHEME-II on the uniform and non-uniform grids yields similar numerical solutions. SCHEME-I on the non-uniform grids produces strong numerical fluctuations initially (before $x/D < 10$) and then departs the numerical solution significantly from the other two.

The terrible behavior of SCHEME-I in figures 10 and 11 is consistent with the analysis of the scheme properties in Section 3. The behavior of SCHEME-I in figure 11 is similar to the behavior of SCHEME-IA and SCHEME-IB in figure 7 to produce the numerical oscillations upstream. In the current simulations with the non-uniform grid, the grid spacing is expanded in the axial flow direction. For such cases, SCHEME-I contains a second-order numerical diffusion term which is anti-dissipative (Section 2.3) and adds energy into the numerical solutions (Section 2.6), and hence produces the excessive numerical oscillations. In contrast, SCHEME-II is free of the second-order numerical diffusion and energy-production, and hence the numerical accuracy and the smoothness is well preserved in the numerical solution.

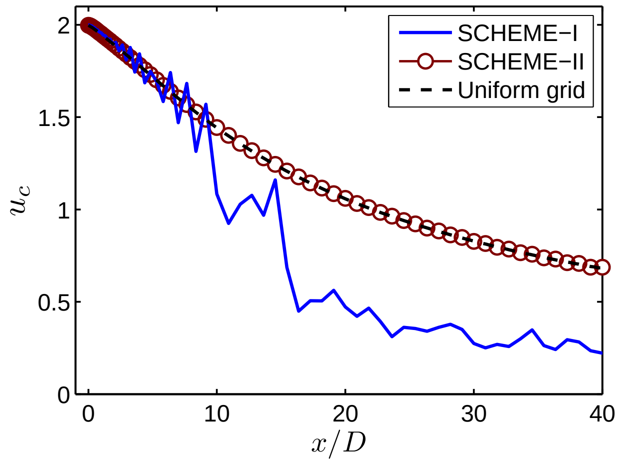

Figure 11: Axial profiles of the centerline axial velocity u_c in the laminar jet flow with non-uniform grid (SCHEME-I and SCHEME-II) and with uniform grid.

Thus, SCHEME-I is not suitable for the numerical simulations of laminar jet flows on stretched (non-uniform) grids, while SCHEME-II is capable of reproducing the smooth numerical solutions accurately. Next we compare the different schemes in LES of turbulent jet flows.

5. LES of a constant-density turbulent jet

5.1. Simulation details

LES simulations are performed of the constant-density turbulent free jet flow measured by Amielh et al. [41]. The self-similar region and the near field are measured for both constant and variable density jets. The detailed measurements of the velocity and turbulence fields, especially in the near filed, provide an excellent test case for the comparison of the different schemes which effect is most sensitive in the near field of the jet. Only the constant-density air jet is considered here. The flow set-up consists of a round air jet with diameter $D = 26mm$ which issues with fully developed pipe flow condition into a low speed air coflow. The Reynolds number of the jet is Re=21000. The mean jet inlet velocity at the centerline $U_j = 12m/s$ and the coflow velocity is $U_e = 0.9231m/s$.

The LES simulations are performed on a cylinder $[0, 60D] \times [0, 8D] \times [0, 2\pi]$ in the axial, radial, and azimuthal directions. Three different grids are used in the simulations ($n_x \times n_y \times n_z$=96×64×48, 144×96×72, and 288×192×144, where n_x, n_y and n_z denote the number of grid cells in the axial, radial and azimuthal directions, respectively) for the comparison of SCHEME-I (70) and SCHEME-II (71) and for the study of the convergence of the results with respect to the grid refinement. The n_x grid cells in the axial direction are stretched in the axial flow direction, yielding the smallest grid spacing at the jet inlet and the largest grid spacing at the outflow plane, and the ratio 16 of the largest and smallest grid sizes. In the radial direction, the grid spacing is clustered near the axis and the jet pipe. A uniform grid is used in the periodic azimuthal direction. A separate LES simulation of a fully developed turbulent pipe flow is performed beforehand and the results are stored in a database to supply the inlet boundary conditions for the jet simulation. The convective boundary condition [14, 20] is used in the lateral and outflow boundaries. The time-step size is controlled by $\mathrm{CFL}_{\max} = 0.5$ for the time advancement on all the grids. The simulations are initiated on the coarsest grid $96 \times 64 \times 48$ from scratch, and the simulations are marched in time until a statistically-stationary state is achieved. Once the numerical results are obtained on the first gird, they are interpolated to the other finer grids as initial conditions. After the statistically-stationary state is reached, the statistics are accumulated by performing time-averaging for about five flow-through times (based on the mean jet inlet velocity) for all grids. Longer time-averaging is not found to affect the statistics.

5.2. Statistics

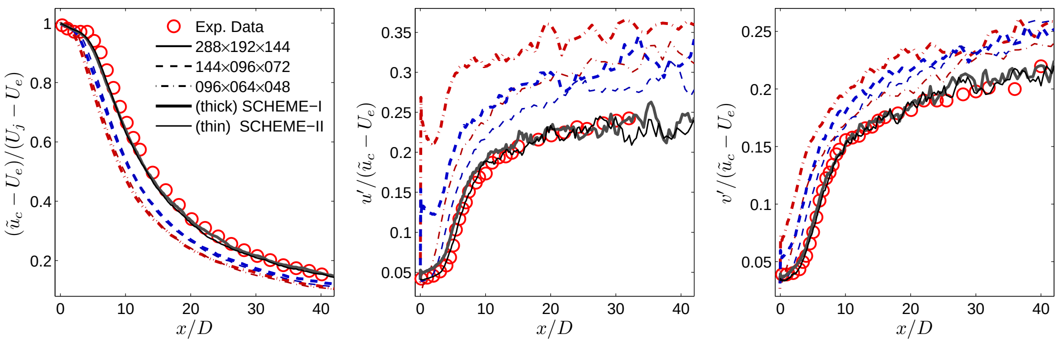

Figure 12: Axial profiles of the normalized centerline axial velocity $(\tilde{u}_c - U_e)/(U_j - U_e)$, turbulence intensities $u'/(\tilde{u}_c - U_e)$ and $v'/(\tilde{u}_c - U_e)$ in the turbulent jet flow with the different grids and with the different schemes (SCHEME-I and SCHEME-II). (The combination of the line styles and the line width denotes a test case, e.g., the thick dashed line denotes the test case on grid $144 \times 096 \times 072$ with SCHEME-I.)

The profiles of the statistics from the LES of the turbulent jet are examined first. In figure 12 are shown the axial profiles of the normalized centerline axial velocity $(\tilde{u}_c - U_e)/(U_j - U_e)$, turbulence intensities $u'/(\tilde{u}_c - U_e)$ and $v'/(\tilde{u}_c - U_e)$ with the different grids and with the different schemes (SCHEME-I and SCHEME-II). From figure 12, we can see that the effect of the different schemes on the centerline axial velocity is slight, while the effect on the centerline turbulence intensities are dramatic, especially on the axial turbulence intensity u' in the near field ($x/D < 10$) on the axis. SCHEME-I significantly overpredicts the turbulent fluctuations on the axis compared to SCHEME-II on the same grid. As we have discussed before, SCHEME-I introduces an energy production term on the current non-uniform grid expanding in the flow direction and consistently adds energy into the numerical solution, which precisely explains the significant overprediction of u' and v' by SCHEME-I. The strong sensitivity of the centerline LES results to the grid refinement is evident as shown in figure 12. With the same scheme on the same grid, the axial velocity decay rate and the turbulence intensities tend to be overpredicted on the relative coarse grids. When the grids are refined, the numerical results show monotonic convergence to the experimental data [41] for the same scheme. The difference between SCHEME-I and SCHEME-II also decreases as the grids are refined, which suggests that SCHEME-I and SCHEME-II converge to the same asymptotic solutions. With the finest grid $288 \times 192 \times 144$, the results of both schemes are in excellent agreement with the experimental data [41] on the axis.

The radial profiles are shown in figure 13 of the turbulence intensities $u'/(\tilde{u}_c - U_e)$ and $v'/(\tilde{u}_c - U_e)$ and of the shear stress $\widetilde{u'v'}/(\tilde{u}_c - U_e)^2$ at the axial locations x/D=0.2, 2, 5 and 20 in the jet flow with the three different grids and the two different schemes. The radial distance r is normalized by the jet half width $r_{\frac{1}{2}}$. In the figure, the improvements of the results by SCHEME-II compared to SCHEME-I are shown consistently at the all axial locations for all three turbulence quantities on all the grids based on their comparison with the experimental data [41]. The greatest improvement by SCHEME-II occurs for u' on the coarsest grid $96 \times 64 \times 48$ near the axis at x/D=0.2. For the same scheme on the same grid, both schemes tend to overpredict the turbulence intensities and the shear stress on the relative coarse grids at all the locations examined in figure 13 in comparison with the experimental data [41]. With

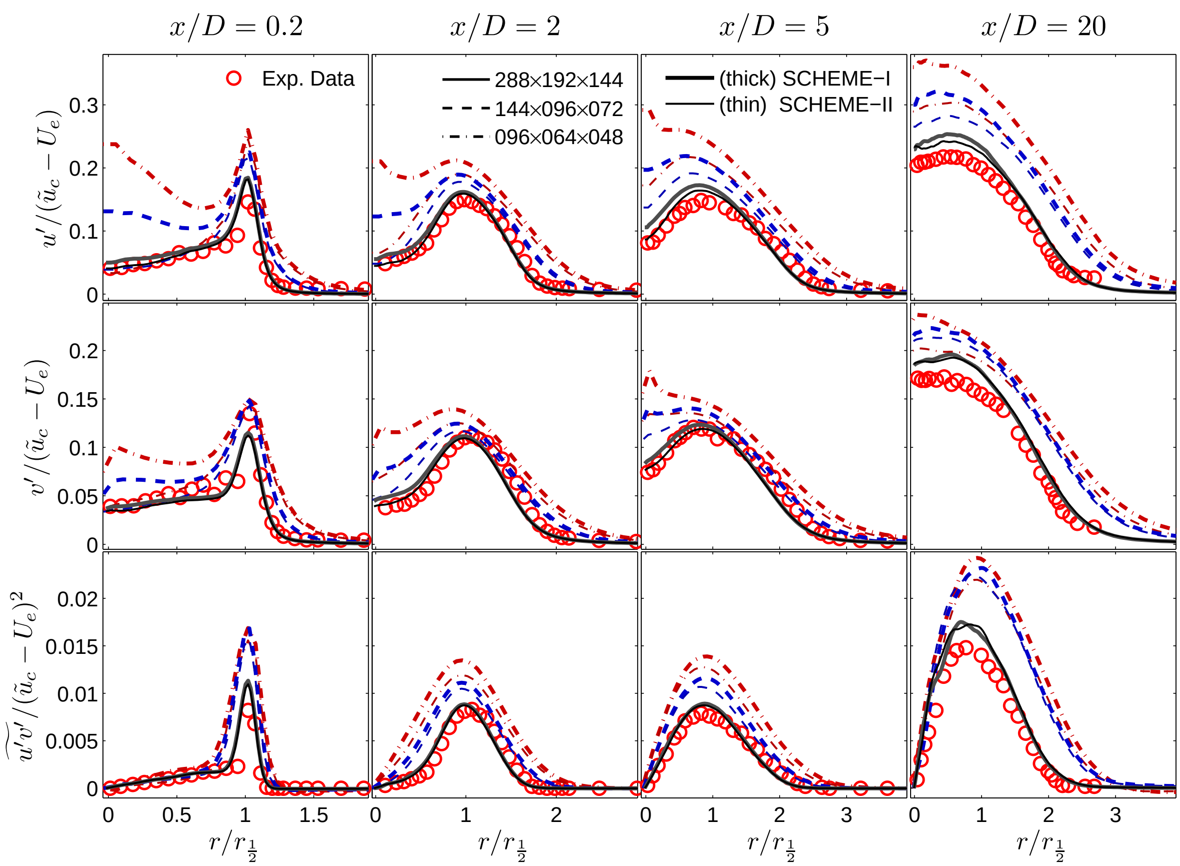

Figure 13: Radial profiles of the normalized turbulence intensities $u'/(\tilde{u}_c - U_e)$ and $v'/(\tilde{u}_c - U_e)$ and the shear stress $\widetilde{u'v'}/(\tilde{u}_c - U_e)^2$ at the different axial locations x/D=0.2, 2, 5 and 20 in the turbulent jet flow with the different grids and with the different schemes (SCHEME-I and SCHEME-II). (The combination of the line styles and the line width denotes a test case, e.g., the thick dashed line denotes the test case on grid $144 \times 096 \times 072$ with SCHEME-I.)

the grids being refined, the difference in the radial profiles by the two schemes decreases, and both profiles converge monotonically to the experimental data [41]. On the finest grid, the radial profiles produced by both schemes agree with the experimental data [41] very well.

5.3. Effect on stability and cost

As shown in Section 5.2 in the above, SCHEME-II is slightly more accurate than SCHEME-I on the same grid. In another words, SCHEME-II can achieve the same numerical accuracy as SCHEME-I but with coarser grids. Hence SCHEME-II reduces the computational cost of the LES simulations.

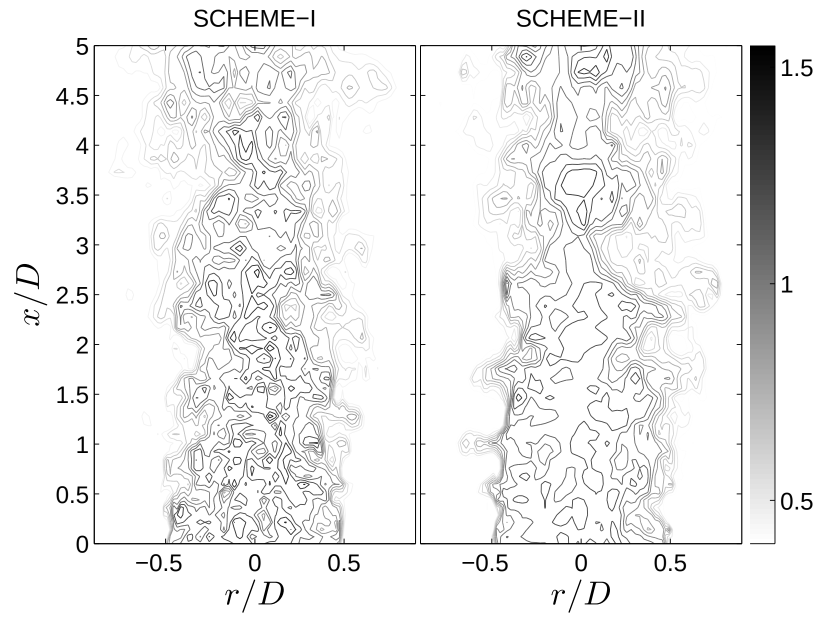

Figure 14: Contour plots of the axial velocity in the near field ($0 \leqslant x/D \leqslant 5$ and $0 \leqslant r/D \leqslant 0.9$) of the turbulent jet flow with SCHEME-I (left) and SCHEME-II (right) on the grid $144 \times 96 \times 72$.

Here we further compare SCHEME-I and SCHEME-II in terms of the numerical stability and the computational cost. The contour plots of the axial velocity in the jet near field are shown in figure 14 with SCHEME-I and SCHEME-II on the grid $144 \times 96 \times 72$. As shown evidently in the figure, SCHEME-I causes excessive numerical fluctuations in the near field, which potentially causes numerical instability. In figure 15, the time series of the maximum resolved axial velocity $\tilde{u}$ in the computational domain and the time step size Δt are monitored after the statistically-stationary state has been reached. SCHEME-I has slightly higher predictions for the $\max(\tilde{u})$ than SCHEME-II. This elevated value of $\max(\tilde{u})$ by SCHEME-I is also dangerous to numerical stability.

On the aspect of the computational cost, we can see from figure 15 that SCHEME-I has smaller size of the time step than SCHEME-II given the same CFL_{max}=0.5 on the same grid. The increased time-step size for SCHEME-II is due to the reduced $\max(\tilde{u})$ which occurs right after the inlet plane near the axis and determines the maximum local CFL number. The average values of the normalized time step size are 0.0204 and 0.0232 for SCHEME-I and SCHEME-II, respectively, which result in approximately 10% increase in the time step size by replacing SCHEME-I with SCHEME-II. Thus, given the same CFL_{max}, SCHEME-II reduces the computational cost by approximately 10% compared to SCHEME-I.

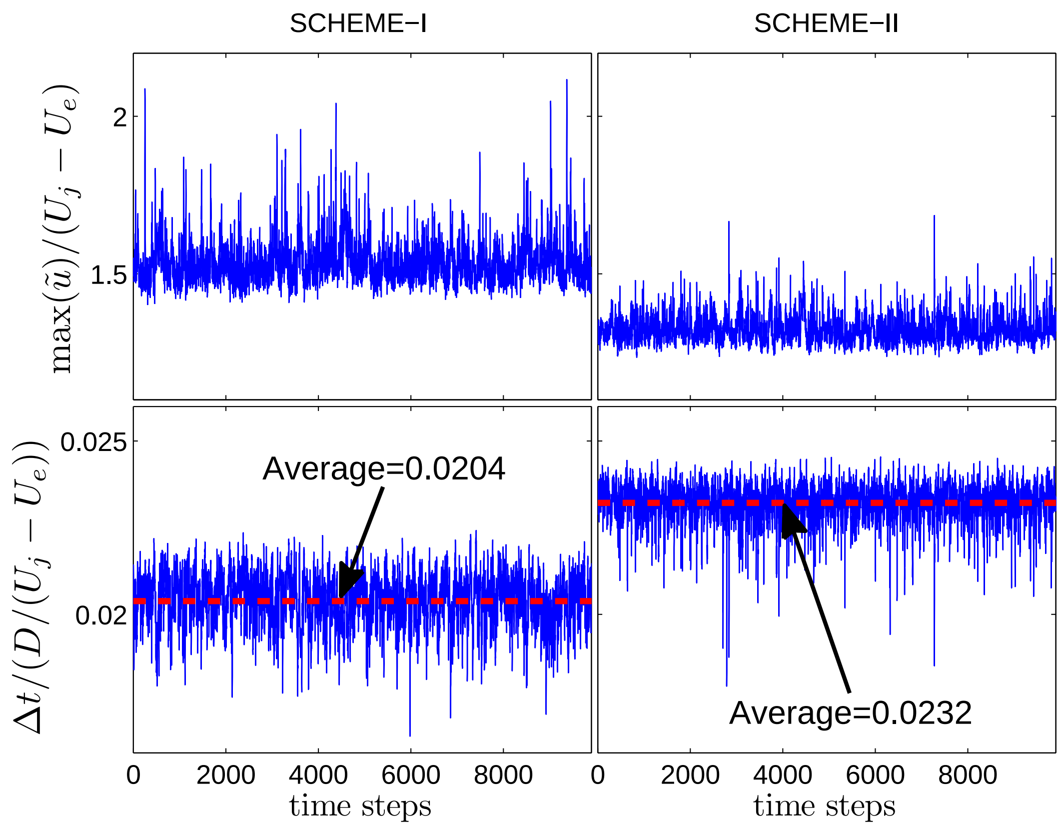

Figure 15: The monitoring of the maximum resolved axial velocity $\tilde{u}$ and the time step size Δt with SCHEME-I (left) and SCHEME-II (right) on the grid $144 \times 96 \times 72$.

To summarize, in this section SCHEME-I and SCHEME-II are compared for the discretization of the non-linear convection terms in the practical LES studies. A constant-density turbulence jet [41] is chosen as a test case. SCHEME-I significantly overpredicts the turbulence fluctuations, while SCHEME-II reproduces the turbulence level very well. Both schemes show monotonic convergence to the experimental data when the grids are refined. The schemes are further compared in terms of the stability and the computational cost, and SCHEME-II is about 10% more efficient than SCHEME-I due to the increased time step size given the same maximum allowed CFL number.

6. LES of turbulent jet flame (DLR Flame A)

In this section, the LES simulations of a turbulent jet flame (DLR Flame A) [42, 43] are performed to further compare SCHEME-I and SCHEME-II. Turbulent combustion is more challenging for LES due to its large density variations and the strong coupling between the turbulence field and the density field. Serious stability problems may be encountered in combustion LES. In practice, most combustion LES are carried out using the low second-order spatial discretization schemes. The performance of the two schemes (SCHEME-I and SCHEME-II) in combustion LES is not known from any previous work.

6.1. Simulation details

The closure of combustion is as hard as the closure of turbulence in LES. In this work, to test the numerical schemes efficiently, we use a simple flamelet combustion model to close the subfilter combustion [34]. Such a model is very attractive in terms of computational economy. The LES simulation details for DLR Flame A have been described in [34], and are only briefly outlined here. DLR Flame A [42, 43] consists of a simple turbulent jet flame of $CH_4/H_2/N_2$ with moderate Reynolds number (Re=15200). The jet nozzle has a diameter of D= 8mm (with bulk velocity U_b=42.2m/s) surrounded by a low-velocity air coflow (U_e=0.3m/s). The fuel consists of 22.1% CH_4, 33.2% H_2, and 44.7% N_2 by volume. The flame exhibits very little local extinction, and hence is suitable for this study using the flamelet model to obtain the thermochemical properties. The mixture fraction transport equations (63) and (64) are solved together with the LES equations for the mass and momentum. The density $\overline{\rho}$ and other quantities (such as temperature $\tilde{T}$ and species mass fractions) are retrieved from a pre-computed flamelet table [34] given the resolved mixture fraction $\tilde{\xi}$ and its subfilter variance $\widetilde{\xi'^2} = \widetilde{\xi^2} - \tilde{\xi}^2$. The molecular transport properties are computed from the empirical fits $\mu/\overline{\rho} = 2.22 \times 10^{-5} \cdot (\tilde{T}/T_0)^{1.66}\mathrm{m}^2/\mathrm{s}$ and $\Gamma = 2.71 \times 10^{-5} \cdot (\tilde{T}/T_0)^{1.69}\mathrm{m}^2/\mathrm{s}$, where T_0=300K [34].

The computational domain is specified to be $[0, 120D] \times [0, 30D] \times [0, 2\pi]$ in the axial, radial and azimuthal directions. Three different grids are used in the simulations ($n_x \times n_y \times n_z$=96×64×48, 144×96×72, and 288×192×144). The n_x grid cells in the axial direction are stretched in the axial flow direction, yielding the smallest grid spacing at the jet inlet and the largest grid spacing at the outflow plane, and the ratio 12 of the largest and smallest grid sizes. In the radial direction, the grid cells are clustered near the axis and the jet pipe. A uniform grid is used in the periodic azimuthal direction. A separate LES simulation of a fully-developed turbulent pipe flow is performed beforehand and the results are stored in a database to supply the inlet boundary conditions for the jet simulation. The convective boundary condition [14, 20] is used in the lateral and outflow boundaries. The time-step size is controlled by $\mathrm{CFL}_{\max} = 0.25$ for the time advancement for all the grids. The numerical results are initially obtained on the coarsest grid $96 \times 64 \times 48$ from scratch and are used as the initial conditions on the subsequent finer grids. The statistics are accumulated for about five flow-through times (based on the mean jet inlet velocity) for all the grids.

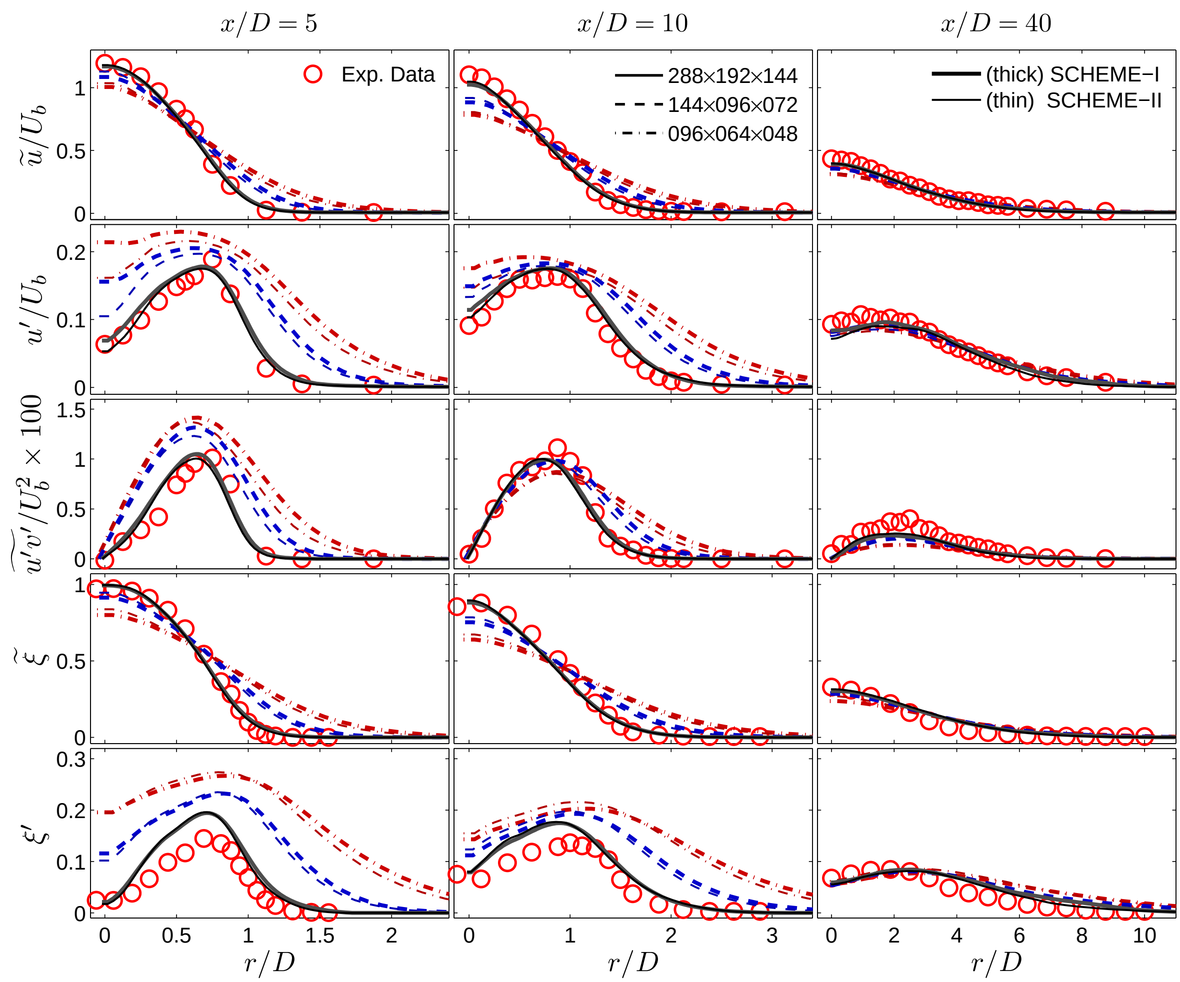

Figure 16: Radial profiles of the axial velocity $\widetilde{u}/U_b$, the axial turbulence intensity u'/U_b, the shear stress $\widetilde{u'v'}/U_b^2$, the mixture fraction $\tilde{\xi}$, and the rms mixture fraction ξ' at the different axial locations x/D=5, 10 and 40 in DLR Flame A with the different grids and with the different schemes (SCHEME-I and SCHEME-II). (The combination of the line styles and line width denotes a test case, e.g., the thick dashed line denotes the test case on grid $144 \times 096 \times 072$ with SCHEME-I.)

6.2. Flow and turbulence fields

The radial profiles of the flow and turbulence fields in DLR Flame A are explored on the three grids ($n_x \times n_y \times n_z$=$96 \times 64 \times 48$, $144 \times 96 \times 72$, and $288 \times 192 \times 144$). In figure 16 are shown the radial profiles of the axial velocity $\widetilde{u}/U_b$, the axial turbulence intensity u'/U_b, the shear stress $\widetilde{u'v'}/U_b^2$, the mixture fraction $\tilde{\xi}$, and the rms mixture fraction ξ' at the axial locations x/D=5, 10 and 40 with the different grids and with the different schemes (SCHEME-I and SCHEME-II). Comparing SCHEME-I and SCHEME-II, we see that the numerical results with SCHEME-II are consistently in better agreement with the experimental data [42, 43] than SCHEME-I for all the locations and all the quantities in figure 16 with only few exceptions, e.g., the rms mixture fraction near the axis at $x/D = 10$. The improvement of the results by SCHEME-II is more evident upstream ($x/D \leq 10$) and less evident downstream ($x/D = 40$) in figure 16. The most significant improvements are observed for u' near the axis at $x/D = 5$, which is similar to the observations in the jet simulation in figure 13. The strong grid dependency of the LES results can also be observed in figure 16, especially upstream. With the grid refinements, the numerical results converge monotonically to the experimental data [42, 43] for both schemes. On the finest grid $288 \times 192 \times 144$, the numerical results of both schemes agree with the experimental data very well. The axial decay rate of the axial velocity and the mixture fraction, and the magnitude of the turbulence intensity, shear stress and the rms mixture fractions are consistently overpredicted on the coarse grid upstream (e.g., x/D=5). When the grids are refined, this magnitude of overprediction is reduced. This overprediction upstream is propagated to the downstream in some non-linear fashion, and can lead to the opposite trend in the downstream, e.g., the shear stress is underpredicted on the coarse grids at $x/D = 10$ and $r/D < 1$.

6.3. Combustion fields

The radial profiles of the resolved mean and rms of the temperature T and the species mass fractions of O_2, CO, and NO are compared in figure 17 at the different axial locations x/D=5, 10 and 40 in DLR Flame A with the different grids and with the different schemes (SCHEME-I and SCHEME-II). These quantities are solely dependent on the mixture fraction for the flamelet model. Similar observations to figure 16 can be made for these scalars, e.g., the improvement by SCHEME-II compared to SCHEME-I and the convergence trend to the experimental data with the grid refinement. On the finest grid $288 \times 192 \times 144$, the numerical results of the both schemes agree with the experimental data [42] very well including the intermediate species CO and the pollutant NO, which validates that the flamelet model used in this study is sufficient for the numerical study.

In summary, SCHEME-I and SCHEME-II are further compared in combustion LES studies. A turbulent jet flame (DLR Flame A) [42, 43] is chosen as a test case. The overall improvements to the LES predictions by SCHEME-II compared to SCHEME-I are evident for this test case including the flow and turbulence fields, and the combustion fields. The convergence of the statistics is also observed for both schemes when the grids are refined.

7. Discussion

SCHEME-I on non-uniform grids introduces a second-order numerical diffusion term in the truncation errors (Section 2.4), so SCHEME-I can be viewed as an upwind-biased or downwind-biased finite-difference scheme depending on the local grid stretching. For grids shrinking in the flow direction, this scheme is dissipative, so it is an upwind-biased scheme; for grids expanding in the flow direction which is focused in this study, the scheme is anti-dissipative, so it is a downwind-biased scheme. As we know, downwind scheme can cause excessive fluctuations and cause numerical instability. SCHEME-II eliminates this second-order numerical diffusion. Another possible way to remedy

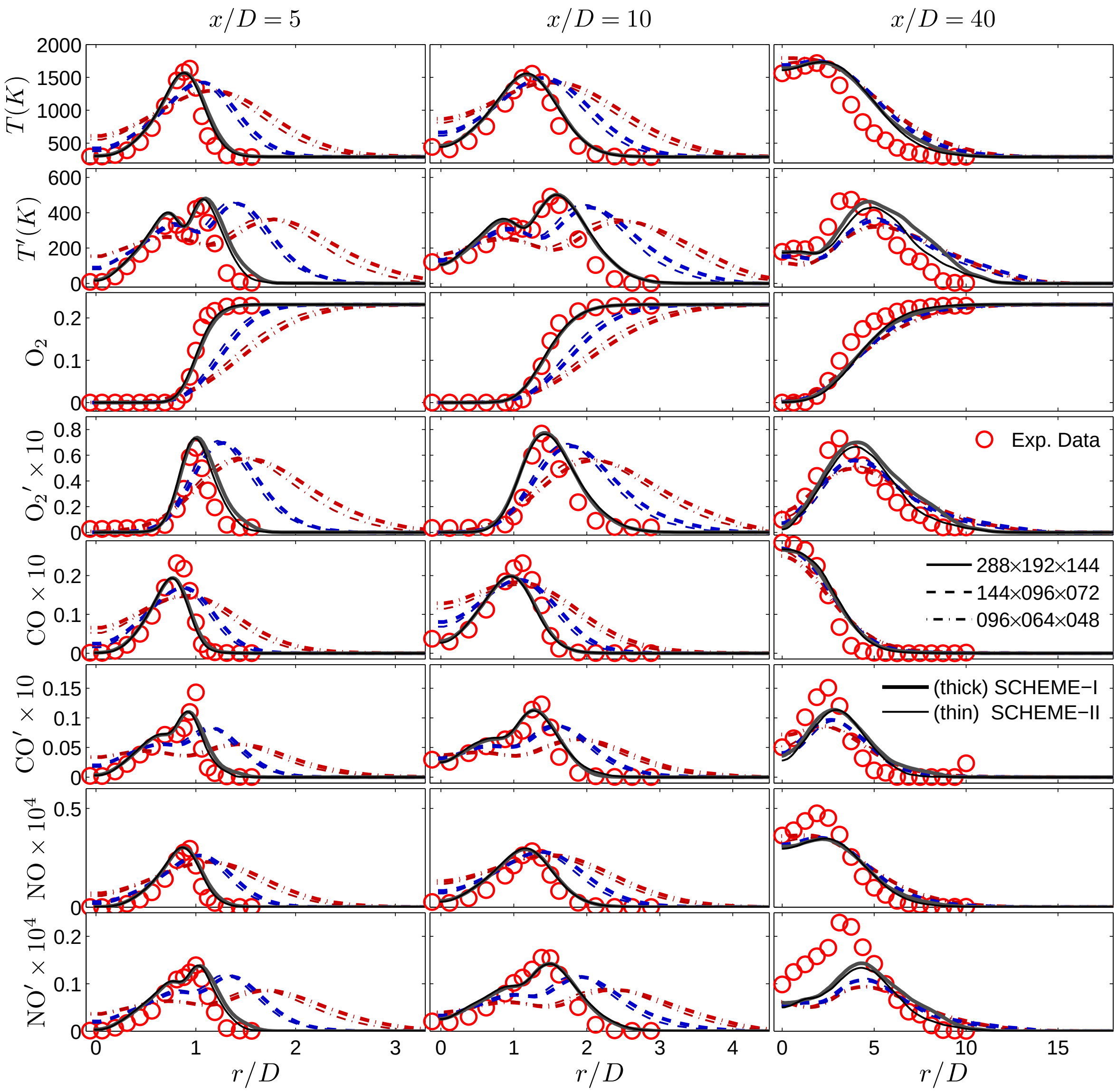

Figure 17: Radial profiles of the resolved mean and rms of the temperature T and the species mass fractions of O_2, CO, and NO at the different axial locations x/D=5, 10 and 40 in DLR Flame A with the different grids and with the different schemes (SCHEME-I and SCHEME-II). (The combination of the line styles and line width denotes a test case, e.g., the thick dashed line denotes the test case on grid $144 \times 096 \times 072$ with SCHEME-I.)

this problem by SCHEME-I is to use upwind-biased schemes. During the study of this work, the upwind schemes (e.g., first-order upwind, QUICK scheme) are tested and they are found to be too dissipative to capture the right physical turbulence fluctuations. As already pointed out by Mittal and Moin [44], upwind-biased finite-difference schemes are not suitable for LES due to their removal of energy in the high wave number. Therefore the idea of using the upwind-biased scheme to suppress the excessive number oscillations is not suitable for the current LES.

The instability of SCHEME-I is not found to be a serious problem for the current study given the local grid stretching rate is not too high, so that the excessive numerical fluctuations can be tolerated by the sub-filter diffusion. Mittal and Moin [44] reported that SCHEME-I can tolerate only a small stretching factor (< %3) in the streamwise flow direction. SCHEME-II discussed in this paper certainly does not have such restriction on the grid stretching for the numerical stability. Due to the numerical oscillations caused by SCHEME-I, the LES results are less accurate than those by SCHEME-II, and the convergence of the results is slower than that by SCHEME-II.

It is desirable for the numerical schemes used in LES to have the property of conservation (for the momentum and energy), and the property of dissipation-free or low dissipation. On non-uniform grid, for second-order accurate schemes, it seems not possible to have a scheme to possess both properties. SCHEME-I guarantee the conservation for momentum and energy, but is highly dissipative or anti-dissipative. SCHEME-II is free of the second-order numerical dissipation, but can not guarantee conservation. Based on the test cases in this work, we see that SCHEME-II is much better than SCHEME-I in terms of avoiding strong numerical oscillations in the numerical solution at the expense of losing conservation. The violation of conservation by SCHEME-II does not cause any serious problems for all the test cases with different levels of complexity considered in this work. By transforming the problem from the physical space to the computational space and discretize the equations in the uniform computational grids, as having been done in several previous works (e.g., [2, 4, 5, 17]), does not resolve the problem as discussed in Appendix B.

8. Conclusion

In this work, the conventional second-order central-difference schemes are revisited. SCHEME-I and SCHEME-II are compared comprehensively for a linear convection problem to understand their numerical properties thoroughly. Both schemes are numerically second-order accurate with carefully specified grids although SCHEME-I has only formally first-order accuracy. SCHEME-I is highly dissipative or anti-dissipative depending on the local grid stretching, while SCHEME-II is dissipation-free. Both schemes are numerically dispersive, and SCHEME-II has lower magnitude of the dispersion truncation errors than SCHEME-I. SCHEME-I conserves momentum and energy, while SCHEME-II conserves neither momentum nor energy. However, SCHEME-I introduces production or dissipation to the energy and hence the numerical solutions oscillate significantly on grids expanding in the flow direction and contain more energy than the exact one in spite of the energy-conservation of the scheme. SCHEME-II is free of the energy production or dissipation.

The two schemes are adapted to the analysis of the inviscid Burgers' equation. Three schemes are considered: SCHEME-IA (momentum-conservative but not energy-conservative), SCHEME-IB (momentum-conservative and energy-conservative), and SCHEME-II (neither momentum-conservative nor energy-conservative). The schemes are compared in a periodic and a non-periodic test problem for the further analysis of the conservation properties of the different schemes. The different conservation properties of the schemes are confirmed by the periodic test problem. For the non-periodic problem, both SCHEME-IA and SCHEME-IB produce strong fluctuations upstream, while SCHEME-II preserves the upcoming constant value very well. The different behaviors of the different schemes are well explained by the modified PDE analysis.

The application of SCHEME-I and SCHEME-II in practical LES is performed. The schemes are first compared in a laminar jet test case. Even for this simple laminar test, SCHEME-I on non-uniform grids produces excessive numerical oscillations and eventually destroys the smooth numerical solutions. SCHEME-II reproduces the smooth laminar numerical solution very well. The two schemes are further compared in LES of a constant-density turbulent jet and a turbulent jet flame. All the LES results by SCHEME-I are improved to some extent by using SCHEME-II. The greatest improvement is for the axial turbulence intensity in the near field, which is significantly overpredicted by SCHEME-I due to its anti-dissipative nature and its adding energy to the numerical solution. The monotonic convergence of the statistics is clearly shown for both test cases and the LES results on the finest grid have a very good agreement with the available experimental data. The numerical stability and the computational cost of SCHEME-I and SCHEME-II are also discussed, and SCHEME-II is slightly less computationally expensive compared to SCHEME-I due to the reduced maximum axial velocity in the domain for the same maximum allowed CFL number. The superiority of SCHEME-II over SCHEME-I is clearly demonstrated in these practical LES simulations.

Acknowledgments

Large parts of the computations in this work are done on Ranger at the Texas Advanced Computing Center at The University of Texas at Austin under project TG-CTS090020. This work was supported in part by Air Force Office of Scientific Research under grant FA-9550-09-1-0047 and in part it is based upon work supported as part of the Combustion Energy Frontier Research Center funded by the U.S. Department of Energy, Office of Science, Office of Basic Energy Sciences under Award Number DE-SC0001198.

Appendix A. Discrete conservations and modified PDEs

As discussed in Sections 2.5 and 2.6, SCHEME-I conserves momentum and energy at the discrete level for the linear convection problem (1). The modified PDEs (11) and (36) contain the truncation error terms which cannot be expressed in the flux-form as shown in the following, i.e., the rate of change of the total momentum and energy is not solely due to the boundary values. This leads to inconsistency between the discrete level conservation and the modified PDE for SCHEME-I. In the following, we reconcile the discrete momentum and energy conservations and the modified PDEs for SCHEME-I.

The modified PDEs (11) and (36) have terms containing the grid spacing Δx_i. To make the modified PDEs integrable, we need to consider the grid spacing as a continuous function and take the limiting process $\Delta x_i \to 0$. We consider the following transformation

$$x_i = X(ih), \tag{A.1}$$

where $h \equiv 1/I$ and $X(\xi)$ is a function to specify the grid. For the grids considered in Section 2, the function form $X(\xi)$ is given in equations (14) and (17). From equation (A.1) and using the Taylor series expansion, we can write

$$\begin{aligned}
\Delta x_i &= x_i - x_{i-1} = hX' - \frac{h^2}{2}X'' + O(h^3), && \text{(A.2)}\\
\Delta x_{i+1} - \Delta x_i &= x_{i+1} - 2x_i + x_{i-1} = h^2 X'' + O(h^4), && \text{(A.3)}\\
\Delta x_{i+1} + \Delta x_i &= x_{i+1} - x_{i-1} = 2hX' + \frac{h^3}{3}X''' + O(h^5), && \text{(A.4)}\\
\Delta x_i \Delta x_{i+1} &= h^2 X'^2 + O(h^4), && \text{(A.5)}
\end{aligned}$$

where $X' = \partial X/\partial\xi$, $X'' = \partial^2 X/\partial\xi^2$ and $X''' = \partial^3 X/\partial\xi^3$. With the above equations, we can rewrite the modified PDEs (11) and (36) for SCHEME-I as

$$\frac{\partial u}{\partial t} + \frac{\partial u}{\partial x} = -\frac{1}{2}h^2 X'' \frac{\partial^2 u}{\partial x^2} - \frac{1}{6}h^2 X'^2 \frac{\partial^3 u}{\partial x^3} + O\left(h^3\right), \tag{A.6}$$

$$\begin{aligned} \frac{\partial u^2}{\partial t} + \frac{\partial u^2}{\partial x} = & - \frac{1}{2}h^2 X'' \frac{\partial^2 u^2}{\partial x^2} + h^2 X'' \frac{\partial u}{\partial x}\frac{\partial u}{\partial x} \\ & - \frac{1}{6}h^2 X'^2 \left[\frac{\partial^3 u^2}{\partial x^3} - 3\frac{\partial}{\partial x}\left(\frac{\partial u}{\partial x}\frac{\partial u}{\partial x}\right)\right] + O\left(h^3\right). \end{aligned} \tag{A.7}$$

We now view the modified PDEs (A.6) and (A.7) in the continuous sense and we can integrate them over $[0, 2\pi]$ to get

$$\frac{d}{dt}\int_0^{2\pi} u(x,t)dx = u(0,t) - u(2\pi,t) + h^2 \int_0^{2\pi} T_1(x,t)dx, \tag{A.8}$$

$$\frac{d}{dt}\int_0^{2\pi} u^2(x,t)dx = u^2(0,t) - u^2(2\pi,t) + h^2 \int_0^{2\pi} T_2(x,t)dx, \tag{A.9}$$

where all the truncation error terms are grouped into $T_1(x,t)$ and $T_2(x,t)$ which integrations cannot be expressed in terms of the boundary values. Comparing (A.8) and (A.9) with equations (22) and (28), we see that the actual momentum and energy are not conserved exactly by SCHEME-I due to the terms $T_1(x,t)$ and $T_2(x,t)$ in equations (A.8) and (A.9).

The momentum and energy conservations claimed in Sections 2.5 and 2.6 are for the particular total momentum C in equation (24) and the total energy E in equation (30). In the following we explore how the summation $C_I^p = \sum_{i=1}^{I} \frac{1}{2}(u_{i-1}^p + u_i^p)\Delta x_i$ converges to the integral $\int_0^{2\pi} u^p dx$, where $p = 1$ for the momentum ($C = C_I^1$) and $p = 2$ for the energy ($E = C_I^2$). Substituting equation (A.4) into C_I^p, we obtain

$$\begin{aligned} C_I^p &= \frac{1}{2}u_0^p \Delta x_1 + \sum_{i=1}^{I-1} \frac{1}{2}u_i^p (\Delta x_i + \Delta x_{i+1}) + \frac{1}{2}u_I^p \Delta x_I \\ &= \frac{1}{2}u_0^p \Delta x_1 + \sum_{i=1}^{I-1} \frac{1}{2}u_i^p \left(2hX' + \frac{h^3}{3}X''' + O(h^5)\right) + \frac{1}{2}u_I^p \Delta x_I \\ &= \frac{1}{2}u_0^p \Delta x_1 + \sum_{i=1}^{I-1} u_i^p X' h + \frac{h^2}{6}\sum_{i=1}^{I-1} u_i^p \frac{X'''}{X'} X' h + \frac{1}{2}u_I^p \Delta x_I + O(h^4). \end{aligned} \tag{A.10}$$

When the number of grid cells I tends to infinity, the second term in the above equation (A.10) converges to $\int_0^1 u^p X' d\xi = \int_0^{2\pi} u^p dx$, and the third term converges to $(h^2/6)\int_0^{2\pi} u^p (X'''/X')dx$, so we obtain

$$C_\infty^p = \lim_{I\to\infty} C_I^p = \frac{1}{2}u_0^p \Delta x_1 + \int_0^{2\pi} u^p dx + \frac{h^2}{6}\int_0^{2\pi} u^p \frac{X'''}{X'} dx + \frac{1}{2}u_I^p \Delta x_I + O(h^4).$$

From the above analysis, we can see that, for SCHEME-I on non-uniform grid, $\int_0^{2\pi} u^p dx$ are only conserved to $O(h^2)$ due to the exact conservation of C_I^p. This is indeed consistent with the results from the modified PDEs in equations (A.8) and (A.9). Hence the momentum and energy conservations are consistent with the modified PDEs for

SCHEME-I.

Appendix B. Effect of grid transformation

Non-uniform grids are mostly used for treating the non-uniformity of the fields in numerical simulations. The numerical discretization on non-uniform grids is more complicated than that on uniform grids. A second way to deal with non-uniformity is to do grid transformation to convert the problem to an equivalent problem in the computational space in which the uniform grid is used. Using the transformation $x = X(\xi)$ to the linear convection problem (1), we obtain

$$\frac{\partial u}{\partial t} + \frac{1}{X'}\frac{\partial u}{\partial \xi} = 0. \tag{B.1}$$

In the computational space ξ, we use uniform grid $\xi_i = ih$ $(i = 0, \cdots, I)$ where $h = 1/I$. Discretizing the convection term in equation (B.1) with the central-difference scheme, we have the following semi-discretization which we denote as SCHEME-III

$$\frac{du_i}{dt} + \frac{u_{i+1} - u_{i-1}}{2hX'(\xi_i)} = 0. \tag{B.2}$$

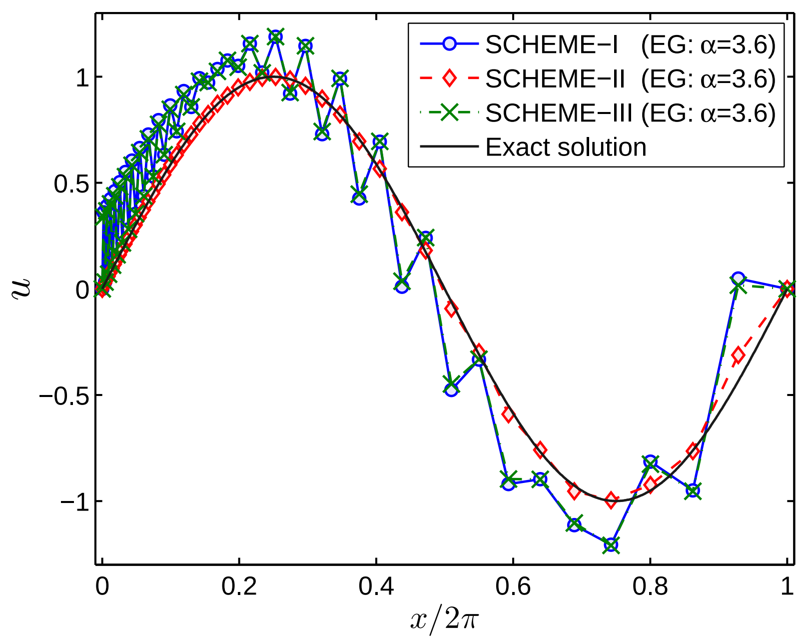

Figure B.18: Numerical solution u at the stopping time $T = 10\pi$ against the position $x/(2\pi)$ with SCHEME-I, SCHEME-II and SCHEME-III (B.2) on the EG grid in equation (14) for Problem-II.

The same numerical test shown in figure 3 is performed using SCHEME-III (B.2). The numerical results are shown in figure B.18 and are compared with those by SCHEME-I and SCHEME-II. The strong numerical oscillation exhibited in the results by SCHEME-I is also observed in the results by SCHEME-III with grid transformation. No significant improvement is found in the results by SCHEME-III (B.2) compared to applying SCHEME-I directly to equation (1). The modified PDE for SCHEME-III (B.2) can be derived as follows,

$$\frac{\partial u}{\partial t} + \frac{\partial u}{\partial x} = -\frac{h^2}{6X'}\frac{\partial^3 u}{\partial \xi^3} + O(h^4). \tag{B.3}$$

Using the chain rule $\partial u/\partial\xi = X'\partial u/\partial x$, we can write the above equation in the physical space x,

$$\frac{\partial u}{\partial t} + (1 + \frac{h^2}{6X'}X''')\frac{\partial u}{\partial x} = -\frac{h^2}{2}X''\frac{\partial^2 u}{\partial x^2} - \frac{h^2}{6}X'^2\frac{\partial^3 u}{\partial x^3} + O(h^4). \tag{B.4}$$

As we can see from the equation, the modified PDE for SCHEME-III (B.2) also contains a numerical diffusion term (the first term on the righthand side of (B.4)) and the term is in the same magnitude as that in the modified PDE (A.6) for SCHEME-I, so it is not a surprise to observe the similar performance of SCHEME-III to SCHEME-I in figure B.18.

Appendix C. Effect of downstream boundary treatments

For solving the hyperbolic problem (1) with the Dirichlet BC (3) (problem-II), only one physical BC upstream is needed. However, for the numerical solution the numerical treatment of the downstream boundary is needed since the central difference schemes are used for the hyperbolic problem. In the discussions in Section 2, the exact solution at the downstream boundary is used for the numerical solutions, i.e., an additional Dirichlet BC (13) is numerically imposed downstream. In this appendix, we explore other downstream boundary treatments and evaluate their effect on the numerical solutions of the hyperbolic problem.

We consider two other downstream boundary treatments. One is to use the first-order upwind scheme for the last grid point I,

$$\frac{du_I}{dt} + \frac{u_I - u_{I-1}}{\Delta x_I} = 0, \tag{C.1}$$

and the other is to extrapolate (with second-order accuracy) the value at the last grid point from the interior grid points,

$$u_I = u_{I-1} + \frac{\Delta x_I}{\Delta x_{I-1}}(u_{I-1} - u_{I-2}). \tag{C.2}$$

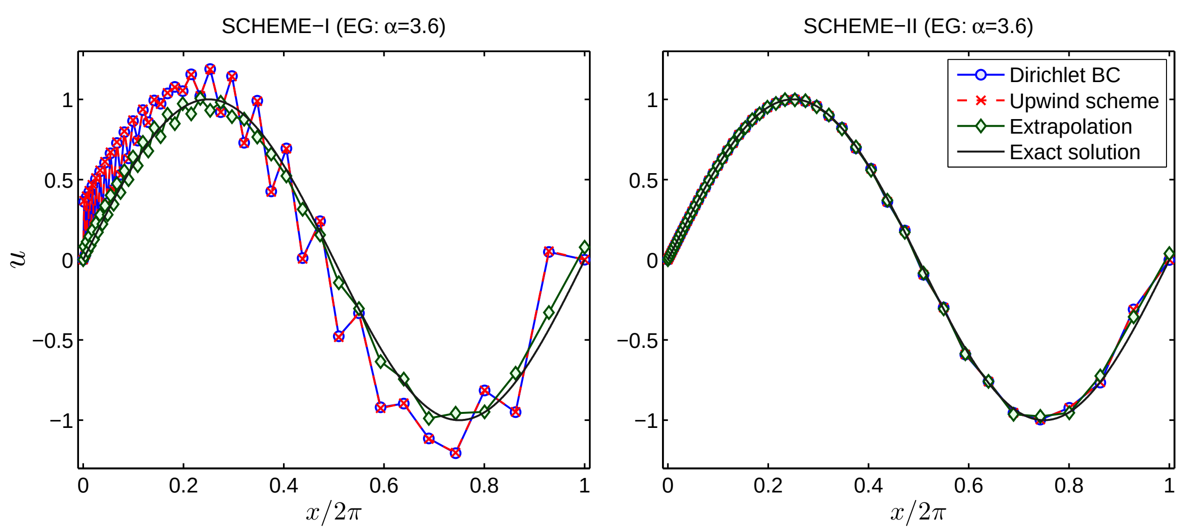

Figure C.19: Numerical solution u at the stopping time $T = 10\pi$ against the position $x/(2\pi)$ with SCHEME-I and SCHEME-II on the EG grid in equation (14) for Problem-II with the different downstream boundary treatments.

The different downstream boundary treatments are compared in figure C.19. In the figure, the same test case as in figure 3 is used. Using upwind scheme (C.1) yields almost the same numerical results as those using the Dirichlet BC (13) downstream for both SCHEME-I and SCHEME-II. The extrapolation (C.2) suppresses the oscillation caused by SCHEME-I to some extent due to the constraint of the last three points lying on a straight line. The different downstream treatments for problem-II do not change the qualitative behavior of the numerical results by the two numerical schemes, i.e., strong oscillations in the results by SCHEME-I and the smooth results by SCHEME-II.

References

[1] Y. Morinishi, T. S. Lund, O. V. Vasilyev, P. Moin, Fully conservative higher order finite difference schemes for incompressible flow, J. Comput. Phys. 143 (1998) 90–124.

[2] O. V. Vasilyev, High order finite difference schemes on non-uniform meshes with good conservation properties, J. Comput. Phys. 157 (2000) 746–761.

[3] F. Nicoud, Conservative high-order finite-difference schemes for low-Mach number flows, J. Comput. Phys. 158 (2000) 71–97.

[4] Y. Morinishi, O. V. Vasilyev, T. Ogi, Fully conservative finite difference scheme in cylindrical coordinates for incompressible flow simulations, J. Comput. Phys. 197 (2004) 686–710.

[5] O. Desjardins, G. Blanquart, G. Balarac, H. Pitsch, High order conservative finite difference scheme for variable density low Mach number turbulent flows, J. Comput. Phys. 227 (2008) 7125–7159.

[6] S. Nagarajan, S. K. Lele, J. H. Ferziger, A robust high-order compact method for large eddy simulation, J. Comput. Phys. 191 (2003) 392–419.

[7] S. K. Lele, Compact finite difference schemes with spectral-like resolution, J. Comput. Phys. 103 (1992) 16–42.

[8] O. Shishkina, C. Wagner, A fourth order finite volume scheme for turbulent flow simulations in cylindrical domains, Computers & Fluids 36 (2007) 484–497.

[9] S. Ghosal, An analysis of numerical errors in large-eddy simulations of turbulence, J. Comput. Phys. 125 (1996) 187–206.

[10] N. Park, K. Mahesh, Analysis of numerical errors in large eddy simulation using statistical closure theory, J. Comput. Phys. 222 (2007) 194–216.

[11] H. Choi, P. Moin, J. Kim, Turbulent drug reduction: studies of feedback control and flow over riblets, Tech. Rep. Report TF-55, Stanford: ThermoScience Division, Department of Mechanical Engineering (1992).

[12] J. G. M. Eggels, F. Unger, M. H. Weiss, J. Westerweel, R. J. Adrian, R. Friendrich, F. T. M. Nieuwstadt, Fully developed turbulent pipe flow: a comparison between direct numerical simulation and experiment, J. Fluid Mech. 268 (1994) 175–209.

[13] F. H. Harlow, J. E. Welch, Numerical calculation of time-dependent viscous incompressible flow of fluid with free surface, Phys. Fluids 8 (12) (1965) 2182–2189.

[14] C. D. Pierce, Progress-variable approach for large-eddy simulation of turbulent combustion, Ph.D. thesis, Stanford University (2001).

[15] C. Wall, C. D. Pierce, P. Moin, A semi-implicit method for resolution of acoustic waves in low Mach number flows, J. Comput. Phys. 181 (2002) 545–563.

[16] F. E. Ham, F. S. Lien, A. B. Strong, A fully conservative second-order finite difference scheme for incompressible flow on nonuniform grids, J. Comput. Phys. 177 (2002) 117–133.

[17] K. Fukagata, N. Kasagi, Highly energy-conservative finite difference method for the cylindrical coordinate system, J. Comput. Phys. 181 (2002) 478–498.

[18] K. Akselvoll, P. Moin, Large-eddy simulation of turbulent confined coannular jets, J. Fluid Mech. 315 (1996) 387–411.

[19] B. J. Boersma, G. Brethouwer, F. T. M. Nieuwstadt, A numerical investigation on the effect of the inflow conditions on the self-similar region of a round jet, Phys. Fluids 10 (4) (1998) 899–909.

[20] C. D. Pierce, P. Moin, Progress-variable approach for large-eddy simulation of non-premixed turbulent combustion, J. Fluid Mech. 504 (2004) 73–97.

[21] A. Dejoan, M. A. Leschziner, Large eddy simulation of a plane turbulent wall jet, Phys. Fluids 17 (2005) 025102.

[22] P. Wang, J. Frohlich, V. Michelassi, W. Rodi, Large-eddy simulation of variable-density turbulent axisymmetric jets, Int. J. Heat Fluid Flow 29 (2008) 654–664.

[23] J. Kim, H. Choi, Large eddy simulation of a circular jet: effect of inflow conditions on the near field, J. Fluid Mech. 620 (2009) 383–411.

[24] H. Pitsch, H. Steiner, Large-eddy simulation of a turbulent piloted methane/air diffusion flame (Sandia flame D), Phys. Fluids 12 (10) (2000) 2541–2554.

[25] H. Pitsch, L. D. de Lageneste, Large-eddy simulation of premixed turbulent combustion using a level-set approach, Proc. Combust. Inst. 29 (2002) 2001–2008.

[26] V. Raman, H. Pitsch, Large-eddy simulation of a bluff-body-stabilized non-premixed flame using a recursive filter-refinement procedure, Combust. Flame 142 (2005) 329–347.
[27] R. Mustata, L. Valino, C. Jimenez, W. P. Jones, S. Bondi, A probability density function Eulerian Monte Carlo field method for large eddy simulations: Application to a turbulent piloted methane/air diffusion flame (andia D), Combust. Flame 145 (2006) 88–104.
[28] H. El-Asrag, S. Menon, Large eddy simulation of bluff-body stabilized swirling non-premixed flames, Proc. Combust. Inst. 31 (2007) 1747–1754.
[29] S. James, J. Zhu, M. S. Anand, Large eddy simulations of turbulent flames using the filtered density function model, Proc. Combust. Inst. 31 (2007) 1737–1745.
[30] V. Raman, H. Pitsch, A consistent LES/filtered-density function formulation for the simulation of turbulent flames with detailed chemistry, Proc. Combust. Inst. 31 (2007) 1711–1719.
[31] M. Wang, J. Huang, W. K. Bushe, Simulation of a turbulent non-premixed flame using conditional source-term estimation with trajectory generated low-dimensional manifold, Proc. Combust. Inst. 31 (2007) 1701–1709.
[32] A. W. Vreman, B. A. Albrecht, J. A. van Oijen, L. P. H. de Goey, R. J. M. Bastiaans, Premixed and nonpremixed generated manifolds in large-eddy simulation of Sandia flame D and F, Combust. Flame 153 (2008) 394–416.
[33] M. Ihme, H. Pitsch, D. Bodony, Radiation of noise in turbulent non-premixed flames, Proc. Combust. Inst. 32 (2009) 1545–1553.
[34] H. Wang, S. B. Pope, Large eddy simulation/probability density function modeling of a turbulent $CH_4/H_2/N_2$ jet flame, Proc. Combust. Inst. 33 (2011) 1319–1330.
[35] H. J. Crowder, C. Dalton, Errors in the use of nonuniform mesh systems, J. Comput. Phys. 7 (1971) 32–45.
[36] E. K. de Rivas, On the use of nonuniform grids in finite-difference equations, J. Comput. Physics 10 (1972) 202–210.
[37] J. D. Hoffman, Relationship between the truncation errors of centered finite-difference approximations on uniform and nonuniform meshes, J. Comput. Phys. 46 (1982) 469–474.
[38] A. E. P. Veldman, K. Rinzema, Playing with nonuniform grids, J. Engi. Math. 26 (1992) 119–130.
[39] P. de Oliveira, F. Patricio, Numerical oscillations on nonuniform grids, J. Eng. Math. 31 (1997) 319–335.
[40] J. H. Ferziger, M. Peric, Computational Methods for Fluid Dynamics, 3rd Edition, Springer, 2002.
[41] M. Amielh, T. Djeridane, F. Anselmet, L. Fulachier, Velocity near-field of variable density turbulent jets, Int. J. Heat Mass Transfer 39 (10) (1996) 2149–2164.
[42] W. Meier, R. S. Barlow, Y.-L. Chen, J.-Y. Chen, Raman/Raleigh/LIF measurements in a turbulent $CH_4/H_2/N_2$ jet diffusion flame: Experimental techniques and turbulence-chemistry-interaction, Combust. Flame 123 (2000) 326–343.
[43] C. Schneider, A. Dreizler, J. Janicka, Flow field measurements of stable and locally extinguishing hydrocarbon-fuelled jet flames, Combust. Flame 135 (2003) 185–190.
[44] R. Mittal, P. Moin, Suitability of upwind-biased finite difference schemes for large-eddy simulation of turbulent flows, AIAA J. 35 (8) (1997) 1415–1417.